

Probing the primordial initial mass function with high- z supernovae

R. S. de Souza^{1,2*}; E. E. O. Ishida^{3,4}; D. J. Whalen^{5,6}; J. L. Johnson⁵; A. Ferrara⁷

¹Korea Astronomy & Space Science Institute, Daejeon 305-348, Korea

²MTA Eötvös University, EIRSA "Lendulet" Astrophysics Research Group, Budapest 1117, Hungary

³Max-Planck-Institut für Astrophysik, Karl-Schwarzschild-Str. 1, D-85748 Garching, Germany

⁴IAG, Universidade de São Paulo, Rua do Matão 1226, 05508-900, São Paulo, Brazil

⁵Los Alamos National Laboratory, Los Alamos, NM 87545, USA

⁶Universität Heidelberg, Zentrum für Astronomie, Institut für Theoretische Astrophysik, Albert-Ueberle-Str. 2, 69120 Heidelberg, Germany

⁷Scuola Normale Superiore, Piazza dei Cavalieri 7, 56126 Pisa, Italy

Accepted – Received –

ABSTRACT

The first supernovae will soon be visible at the edge of the observable universe, revealing the birthplaces of Population III stars. With upcoming near-infrared missions, a broad analysis of the detectability of Population III supernovae is paramount. We combine cosmological and radiation transport simulations, instrument specifications, and survey strategies to create synthetic observations of primeval core-collapse, Type II_n and pair-instability supernovae with the *James Webb Space Telescope* (*JWST*). We show that a dedicated observational campaign with the *JWST* can detect up to ~ 15 pair-instability explosions, ~ 300 core-collapse supernovae, but less than one Type II_n explosion per year, depending on the Population III star formation history. Our synthetic survey also shows that $\approx 1 - 2 \times 10^2$ supernovae detections, depending on the accuracy of the classification, are sufficient to discriminate between a Salpeter and flat mass distribution for primordial stars with a confidence level greater than 99.5 per cent.

Key words: supernovae: general; cosmology: first stars; infrared: general

1 INTRODUCTION

The emergence of Population III (Pop III) stars ended the cosmic dark ages and began the production of elements heavier than lithium (Karlsson et al. 2013). But because Pop III stars have never been observed, their properties remain uncertain. Even detections of Pop III stars through strong gravitational lensing are very unlikely (Rydberg et al. 2013), so it may be decades before they are directly observed. The most viable strategy for probing the properties of the first stars is direct detection of their gamma-ray bursts (GRBs; Bromm & Loeb 2006; de Souza et al. 2011, 2012; Campisi et al. 2011; Nagakura et al. 2012; Mesler et al. 2013) and supernovae (SNe; Kasen et al. 2011; de Souza et al. 2013b; Whalen et al. 2013a). Pop III SNe may soon be found in deep-field surveys by the *James Webb Space Telescope* (*JWST*)¹ and all-sky surveys by *Euclid*² (e.g., Whalen et al. 2013h; Johnson et al. 2013), providing unprecedented insights into cosmic evolution (Bromm 2013) and the properties of primordial mini-haloes (e.g., Whalen et al. 2008; Biffi & Maio 2013; de Souza et al. 2013a,c).

The *JWST* will be an infrared-optimized space telescope with four instruments, the Near-Infrared Camera (NIRCam), the Near-Infrared Spectrograph, the near-infrared Tunable Filter Imager and the Mid Infrared Instrument, with enough fuel for a 10-yr mission (Gardner et al. 2006). Our analysis is based on NIRCam photometry in the 0.6–5 μm bands, one of whose science goals is the exploration of the end of the dark ages. Complementary all-sky searches will also be possible with other NIR missions such as the *Wide-Field Infrared Survey Telescope* (*WFIRST*), the *Wide-field Imaging Surveyor for High-redshift* (*WISH*) and *Euclid*. Pop III SNe will also be visible in the radio at 21 cm to the *Expanded Very Large Array* (eVLA), *eMERLIN* and future radio facilities like the *Square Kilometre Array* (Meiksin & Whalen 2013).

The quest for the first stars has been further motivated by the discovery of pair-instability (PI) SN candidates SN 2007bi at $z = 0.127$ (Gal-Yam et al. 2009; Young et al. 2010) and SN 2213-1745 at $z = 2.06$ (Cooke et al. 2012) and the pulsational pair-instability (PPI) SN candidate SN 1000+0216 at $z = 3.90$ (Cooke et al. 2012). These lower redshifts are less favorable to the formation of massive progenitors than in the early universe. There is also evidence that some Pop III stars may be less massive than suggested by previous studies (Abel et al. 2002; Omukai & Palla 2003; Yoshida et al. 2006). Observationally, there is evidence of

* e-mail: rafael.2706@gmail.com (RSS)

¹ <http://www.jwst.nasa.gov>

² <http://www.euclid-ec.org/>

2 Pop III initial mass function

15 - 50 M_{\odot} Pop III stars in the fossil abundance record, the ashes of early SNe thought to be imprinted on ancient metal-poor stars (Beers & Christlieb 2005; Frebel et al. 2005; Cayrel et al. 2004; Iwamoto et al. 2005; Lai et al. 2008; Joggerst et al. 2010; Caffau et al. 2012). Recent numerical simulations have produced Pop III stars with masses below 50 M_{\odot} (Greif et al. 2011; Clark et al. 2011; Hosokawa et al. 2011; Stacy et al. 2012), and in some cases as low as $\sim 1 - 5 M_{\odot}$ (Stacy & Bromm 2013). A number of such stars could still be living today.

Pop III stars from 15 - 40 M_{\odot} die as core-collapse (CC) SNe and 85-260 M_{\odot} stars explode as far more energetic PI SNe (Heger & Woosley 2002; Chatzopoulos & Wheeler 2012). If a CC SN shock wave collides with a dense circumstellar shell ejected in an outburst a few years prior to the death of the star, a so-called Type IIn SN (Whalen et al. 2013d). Detection limits in redshift for PI SNe (Weinmann & Lilly 2005; Wise & Abel 2005; Pan et al. 2012; Hummel et al. 2012; Whalen et al. 2013a,b; de Souza et al. 2013b), CC SNe (Mesinger et al. 2006; Whalen et al. 2013c) and Type IIn (Tanaka et al. 2012, 2013; Whalen et al. 2013d) have shown that these events will be visible in the NIR at $z \sim 10 - 30$. There is a great expectation that the hunt for the first stars will soon be prosperous, making our study timely and in synergy with the established literature.

The observable properties of a galaxy, such as color and magnitude, are mainly determined by the initial mass function (IMF) and formation history of its stars. These serve as essential inputs, from which semi-analytical models of galaxy evolution can predict colors and luminosities (e.g., Bastian et al. 2010). Probing the primordial IMF will not only improve our understanding of the early stages of star formation, but also help to uncloak a long lasting puzzle: is the IMF universal or does it evolve over cosmic time? We show that the number of primordial SN detections required to reveal the Pop III IMF is feasible. Such an achievement would be one of the main, ground breaking accomplishments of extragalactic astrophysics in the next decade.

Here, we extend the work of de Souza et al. (2013b, hereafter DS13) in several ways: (i) we include spectral energy distributions (SEDs) for CC and Type IIn SNe, and new PI SN SEDs calculated with improved physics, in particular a better implementation of self-gravity into RAGE code, with a reran of the the red and blue supergiant models (Whalen et al. 2013a,b);³ (ii) we analyze how observational strategies affect the detection rate of each SN type; (iii) we construct a statistical study of the feasibility of constraining the Pop III IMF, and (iv) we present the first application of photometric classification techniques to study how well can we discriminate between different Pop III SNe types. The outline of the rest of this paper is as follows. In Section 2, we discuss our cosmological simulations, and in Section 3 we review our SN light curve (LC) calculations. Survey strategies and our synthetic observations are described in Section 4. In Section 5 we discuss future constraints on the Pop III IMF and our adopted statistics. In Section 6 we discuss how to identify each SN type and how this affects our results, and in Section 7 we present our conclusions.

³ The original models were brighter because self-gravity was not properly implemented in RAGE, and the shocks broke out of the star with too much kinetic energy. We have confirmed that this did not affect any of the conclusions from DS13 on the detectability of these events because the new explosions are still quite visible at $z \sim 20$. The peak luminosities in our newer light curves are in good agreement with those of Kasen et al. (2011); Dessart et al. (2013).

2 COSMOLOGICAL SIMULATIONS

The SN rate is directly related to the cosmic star formation rate (SFR), which largely depends on the ability of primordial gas to cool and condense. Hydrogen molecules (H_2) are the primary coolant in primordial gas clouds, and they are sensitive to the soft ultraviolet background (UVB). The UVB in the H_2 -disassociating Lyman-Werner (LW) bands delays star formation inside mini-haloes, and self-consistent cosmological simulations are required to properly account for this effect. We derive cosmic SFRs from a cosmological N-body, hydro and chemistry simulation (Johnson et al. 2013a) done with a modified version (Schaye et al. 2010) of the smoothed-particle hydrodynamics (SPH) code GADGET (Springel et al. 2001; Springel 2005). The modifications include line cooling in photoionization equilibrium for 11 elements (H, He, C, N, O, Ne, Mg, Si, S, Ca, Fe; Wiersma et al. 2009), prescriptions for SN mechanical feedback and metal enrichment, a non-equilibrium primordial chemistry network, and molecular cooling by H_2 and HD (Abel et al. 1997; Galli & Palla 1998; Yoshida et al. 2006; Maio et al. 2007). The transition from Pop III to Pop II/I SF occurs when the metallicity of the gas in the simulation, Z , exceeds the critical value $Z_{crit} = 10^{-4} Z_{\odot}$ (Omukai & Palla 2001; Bromm et al. 2001; Schneider et al. 2002; Mackey et al. 2003; Tornatore et al. 2007; Maio et al. 2010). The simulation starts from cosmological initial conditions and has a cubic volume 4 Mpc (comoving) on a side with periodic boundary conditions. It includes both dark matter (DM) and gas, with SPH gas and DM particle masses of $1.25 \times 10^3 M_{\odot}$ and $6.16 \times 10^3 M_{\odot}$, respectively. The simulation is launched with an equal number of SPH and DM particles, 684^3 . We adopt the WMAP7 cosmological parameters (Komatsu et al. 2009): $\Omega_m = 0.265$, $\Omega_b = 0.0448$, $\Omega_{\Lambda} = 0.735$, $H_0 = 71 \text{ km s}^{-1} \text{ Mpc}^{-1}$, and $\sigma_8 = 0.81$.

We assume a Salpeter IMF for Pop III stars (Salpeter 1955), with upper and lower limits $M_{upper} = 500 M_{\odot}$ and $M_{lower} = 21 M_{\odot}$, respectively (Bromm & Loeb 2004; Karlsson et al. 2008). The prescriptions for Pop III stellar evolution and chemical feedback track the enrichment of gas by the 11 elements listed above individually (Maio et al. 2007), using nucleosynthetic yields from the explosions of metal-free stars (Heger & Woosley 2002, 2010). We include a LW background from proximate sources and sources outside the simulation volume. The photodissociation rate due to this background is included in the reaction network throughout the run. In addition to the LW background, strong spatial and temporal variations in the LW flux can be produced locally by individual stellar sources (Dijkstra et al. 2008; Ahn et al. 2009), and this effect is included by summing the local LW flux contributions from all star particles. Self-shielding of H_2 to the LW background was implemented with shielding functions from Wolcott-Green et al. (2011).

2.1 SN Rate

Since massive stars have cosmologically short lifetimes, $\approx 30(M/8M_{\odot})^{-2.5} \text{ Myr}$, it is usually assumed that the SN rate, \dot{n}_{SN} , traces the cosmic SFR with redshift. This rate can be derived for a particular mass range (and hence explosion type) from the IMF by

$$\dot{n}_{SN}(z) = SFR(z) \frac{\int_{M_{min}}^{M_{max}} \psi(M) dM}{\int_{15M_{\odot}}^{500M_{\odot}} M \psi(M) dM} \text{ yr}^{-1} \text{ Mpc}^{-3}, \quad (1)$$

where $\psi(M)$ is the Pop III IMF, which we assume to have an either Salpeter ($dN/d\text{Log}M \propto M^{-1.35}$) or flat ($dN/d\text{Log}M \propto M$) slope. In reality, any IMF other than Salpeter is not entirely self-

consistent, since mechanical feedback by SNe, metal enrichment, and the LW background can be dependent on the chosen IMF, and these in turn feed back into the SFR. But since Pop II SFRs are much higher than Pop III rates at $z < 15$, the contribution to feedback from Pop III stars is minor at later epochs. The overall SFR is therefore not very sensitive to the Pop III IMF, except perhaps at $z > 15$. Nevertheless, since most of the SNe occur at lower redshifts, this error is smaller than other astrophysical and numerical uncertainties and is thus subsumed in the wide range of parameters explored here.

The lower and upper limits for CC and PI SNe are $M_{\min} = 15$ and $140 M_{\odot}$ and $M_{\max} = 40$ and $260 M_{\odot}$, respectively. New results from Chatzopoulos & Wheeler (2012) show that Pop III stars down to $\sim 85 M_{\odot}$ may produce PI SNe if they are rapidly rotating, which could increase the PI SN rate by a factor of ~ 4 . Our flat IMF is motivated by recent cosmological simulations of primordial star formation (Greif et al. 2011; Clark et al. 2011; Hirano et al. 2013). The fraction of CC SNe that are Type II α is not well determined but is assumed to be 10^{-3} of all CC SNe. This fraction is in agreement with Tanaka et al. (2012) and current constraints from the *Robotic Optical Transient Search Experiment-IIb* (Quimby et al. 2013).

Fig. 1 shows \dot{n}_{SN} from CC, Type II α and PI SNe for different IMFs and SFRs separately. Model SFR1 refers to the standard SFR, adopted in our previous work (DS13, Johnson et al. 2013a), while model SFR10 is a more optimistic case with an SFR that is ten times higher, to account for numerical and astrophysical uncertainties. Our wide range of parameters aims to bracket the SFRs in the literature (Fig. 2, see also Fig. 3 from Whalen et al. 2013e). These rates come from numerical simulations (Campisi et al. 2011; Maio & Iannuzzi 2011; Wise et al. 2012; Hasegawa & Semelin 2013; Johnson et al. 2013a; Muratov et al. 2013; Pawlik et al. 2013; Xu et al. 2013, see Tornatore et al. 2007; Trenti & Stiavelli 2009 for other SFRs that fall within the range shown here), long-duration GRB rates (Ishida et al. 2011; Robertson & Ellis 2012) and UV-selected galaxies (Robertson et al. 2010). The rates predicted by both observations and simulations vary by about two orders of magnitude from $z \sim 10 - 25$.

The SFRs in most of the models are taken from those of a few protogalaxies in their simulation volumes and are therefore subject to small box statistics. At high redshift, galactic halos are rare and correspond to large peaks in the Gaussian probability distribution of initial fluctuations (Barkana & Loeb 2004). In simulations, periodic boundary conditions are usually assumed, thereby forcing the mean density of the box to be the cosmic mean density. This excludes density modes with wavelengths longer than the box size (4 Mpc in our case) from the simulations and results in an underestimate of the mean number of rare, biased halos. Accounting for these missing modes (Barkana & Loeb 2004), we estimate that the true SFR at $z = 7$ (20) could be larger by a factor of ~ 1.3 (7) if star formation is dominated by atomically cooled haloes, or a factor of ~ 1.1 (2) if star-formation is dominated by haloes cooled by H_2 . The simulations also include a variety of feedback processes that lead to a wide range of evolution in stellar populations over redshift.

3 SN LC MODELS

The SN spectra in our study are calculated in three steps. First, the Pop III star is evolved from the zero-age main sequence to central collapse and then explosion in the one-dimensional (1D) KEPLER stellar evolution code (Weaver et al. 1978; Woosley et al. 2002).

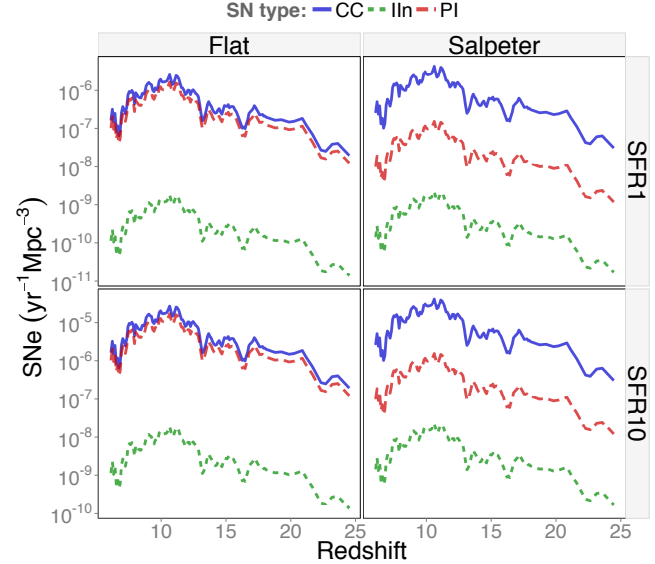


Figure 1. $\dot{n}_{\text{SN}}(z)$ for CC, II α and PI SNe for the two IMFs (columns) and SFRs (rows) as a function of redshift.

Nuclear burning is calculated with a 19-isotope network until oxygen depletion in the core, and with a 128-isotope quasi-equilibrium network thereafter. The KEPLER simulation is halted after the end of explosive burning, when the shock is still deep inside the star. The blast profile, surrounding star, and stellar envelope (a low-density r^{-2} wind profile) are then mapped onto a 1D spherical grid in the Los Alamos RAGE code (Gittings et al. 2008) and evolved through shock breakout from the star and subsequent expansion into the intergalactic medium (IGM). Finally, RAGE profiles are post processed with the Los Alamos SPECTRUM code (Frey et al. 2013) and OPLIB opacities⁴ (Magee et al. 1995) to obtain spectra at 14899 wavelengths. We summarize the properties of our SNe in Table 1.

PI SNe We consider 150, 175, 200, 225, and $250 M_{\odot}$ PI SN progenitors at zero-metallicity (z-series) and $Z = 10^{-4} Z_{\odot}$ (u-series) (Joggerst & Whalen 2011; Whalen et al. 2013b). The u-series stars die as red supergiants and the z-series stars die as compact blue giants. It is generally thought that most stars in this mass range die as red supergiants due to convective mixing over their lives, even at zero metallicity. The onset of the PI and explosion is an emergent feature of the stellar evolution model and does not have to be artificially triggered. PI SNe exhibit little internal mixing that would break the spherical symmetry of the star during the explosion and are generally well-described by 1D models. They make up to 40 M_{\odot} of ^{56}Ni and release up to 10^{53} erg, which powers the LC at intermediate to late times. We evolve these explosions out to 3 yrs because they can be bright out to these times, in part because of the longer radiation diffusion timescales in their massive ejecta. The red supergiants and blue giants in our grid of models bracket the range of structures expected for these stars. Their actual structures, and hence explosion LCs, may be intermediate to those here.

CC SNe The CC SNe in our study are $15 - 40 M_{\odot}$, with explosion energies, E , of 0.6, 1.2, and 2.4×10^{51} erg (the B, D, and G models,

⁴ <http://rdc.llnl.gov>

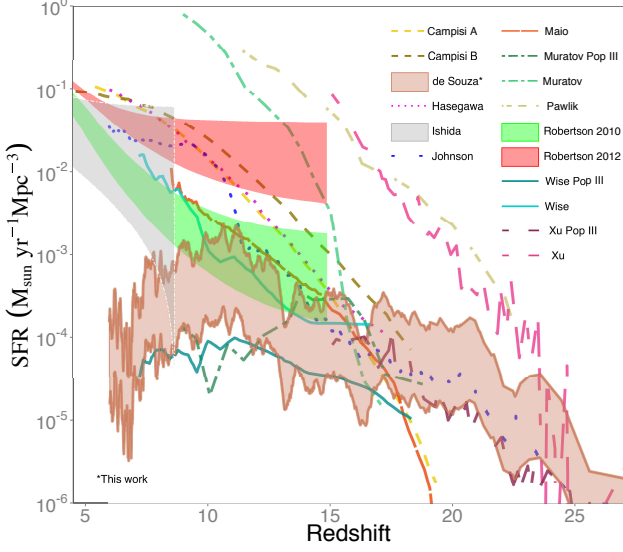


Figure 2. Cosmic SFRs as a function of redshift. The grey and red bands are rates inferred from GRBs (Ishida et al. 2011; Robertson & Ellis 2012) and the green band are rates inferred from UV-selected galaxies (Robertson et al. 2010). The SFRs compiled from simulations are from Campisi et al. (2011); Maio & Iannuzzi (2011); Wise et al. (2012); Hasegawa & Semelin (2013); Johnson et al. (2013a); Muratov et al. (2013); Pawlik et al. (2013); Xu et al. (2013) (see Tornatore et al. 2007; Trenti & Stiavelli 2009, for other SFRs that fall within those shown here). The two lower and upper limits from the salmon band represent the models SFR1 and SFR10 from this work (de Souza et al. 2013b, see also). Boundaries from de Souza, Muratov Pop III, Wise Pop III and Xu Pop III SFR are for Pop III stars only, the others are Pop II + I SFRs.

respectively). They have the same metallicities as our PI SN models and also die as red supergiants (z-series) and compact blue giants (u-series), a total of 18 models. Unlike the PI SNe described above, these explosions must be artificially triggered with linear momentum pistons in KEPLER. Before mapping them to RAGE, these SNe are evolved from the end of explosive burning until just before shock breakout in two dimensions (2D) in the CASTRO adaptive mesh refinement (AMR) code (Almgren et al. 2010). We do this to capture the violent mixing between elemental shells in the star before the SN shock ruptures its surface, as described in Joggerst et al. (2010). These 2D profiles are then averaged in angle, mapped into RAGE, and evolved through shock breakout out to 4 months. Our procedure approximates the order in which absorption and emission lines due to various elements might appear in the 1D spectra over time because of mixing. The structures of these stars again span those expected for Pop III stars in this mass range.

IIn As noted in the Introduction, Type IIn SNe occur when ejecta from a CC explosion crash into a dense shell ejected by the star prior to death. The collision lights up the shell in the UV in the rest frame, whose spectral peak is then redshifted in the NIR at high- z . Such events can be super-luminous because of the large radius of the shell on impact, which can be $\sim 10^{16}$ cm. The star can range in mass from 20 - 40 M_{\odot} , but we adopt the z40G model as our fiducial CC SN and then consider collisions with five shells whose masses are 0.1 - 20 M_{\odot} . These explosions were evolved out to 500 days, past breakout of the shock through the outer surface of the shell.

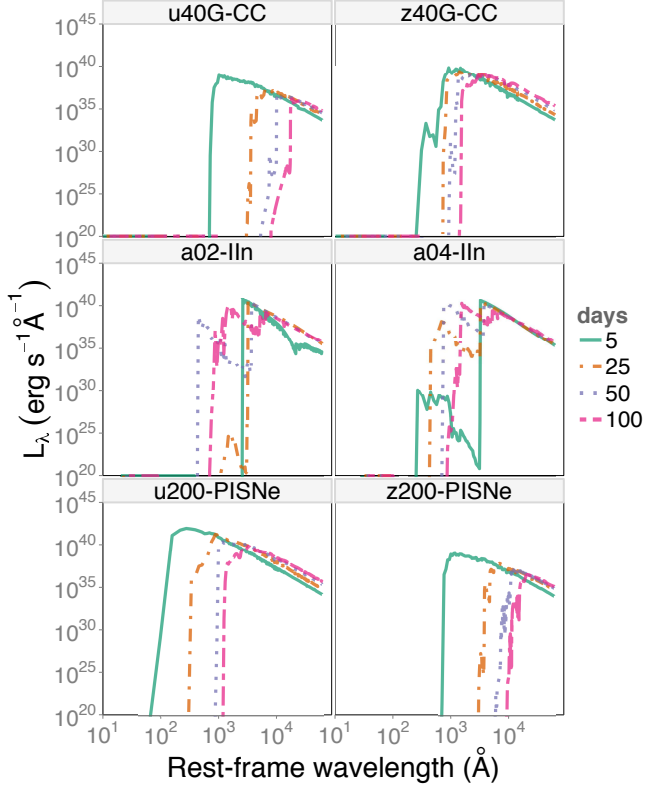


Figure 3. Rest-frame spectral evolution of the u40G and z40G CC SNe, the a02 and a04 Type IIn, and the u200 and z200 PI SNe. Fireball spectra are at ≈ 5 days (green solid line), 25 days (orange dot long-dashed line), 50 days (violet dotted line), and 100 days (pink dot-dashed line).

In Figure 3 we show an example of CC, Type IIn, and PI SN spectral evolution from breakout to 100 days in the rest frame. The evolution of the PI and CC SN SEDs over time is mainly governed by two processes: (i) the fireball expands and cools, and its spectral cutoff advances to longer wavelengths; (ii) the ejecta and envelope, which were ionized by the breakout radiation pulse, begin to recombine and absorb photons at the high energy end of the spectrum, as evidenced by the flux that is blanketed by lines at the short-wavelength limit of the spectrum. At later times, flux at longer wavelengths slowly rises due to the expansion of the surface area of the photosphere. The SEDs are blue at earlier times and become redder at later times as the expanding blast cools. In the Type IIn explosion, the shock driven by the ejecta through the shell causes the jump in luminosity after ~ 30 days. The magnitude of the jump depends on the density of the shell, with diffuse shells allowing more radiation to pass through them.

In Fig. 4 we show LCs in the rest frame and at redshifts 6, 10 and 15 for comparison. The CC SNe exhibit plateaus in the optical bands in the rest frame. But high-redshift Type IIP (CC) SNe do not exhibit plateaus in the NIR because emission in the much bluer bands of origin in the rest frame rapidly declines due to the onset of line opacity at early times in the fireball (compare Fig. 4 with Fig. 7 from Kasen & Woosley (2009), in which the U band flux falls off rapidly in comparison to the plateaus in the I, R and V band fluxes (see also Pan et al. 2012)). The absence of a plateau in the bluer bands in the rest frame of high- z CC SNe is key to their detection in the NIR today. Otherwise, they might not be recognizable as transients.

| Model | SN Type | $M_*(M_\odot)$ | $E(10^{51}\text{erg})$ | $Z(Z_\odot)$ | Model | SN Type | $M_*(M_\odot)$ | $E(10^{51}\text{erg})$ | $Z(Z_\odot)$ |
|-------|---------|----------------|------------------------|--------------|-------|---------|----------------|------------------------|--------------|
| u15B | CC | 15 | 0.6 | 10^{-4} | u150 | PI | 150 | 9.0 | 10^{-4} |
| u25B | CC | 25 | 0.6 | 10^{-4} | u175 | PI | 175 | 21.3 | 10^{-4} |
| u40B | CC | 40 | 0.6 | 10^{-4} | u200 | PI | 200 | 33 | 10^{-4} |
| u15D | CC | 15 | 1.2 | 10^{-4} | u225 | PI | 225 | 46.7 | 10^{-4} |
| u25D | CC | 25 | 1.2 | 10^{-4} | u250 | PI | 250 | 69.2 | 10^{-4} |
| u40D | CC | 40 | 1.2 | 10^{-4} | z175 | PI | 175 | 14.6 | 0 |
| u15G | CC | 15 | 2.4 | 10^{-4} | z200 | PI | 200 | 27.8 | 0 |
| u25G | CC | 25 | 2.4 | 10^{-4} | z225 | PI | 225 | 42.5 | 0 |
| u40G | CC | 40 | 2.4 | 10^{-4} | z250 | PI | 250 | 63.2 | 0 |
| z15B | CC | 15 | 0.6 | 0 | a00 | IIn | $M_{sh} = 0.1$ | 2.4 | 0 |
| z25B | CC | 25 | 0.6 | 0 | a01 | IIn | $M_{sh} = 1.0$ | 2.4 | 0 |
| z40B | CC | 40 | 0.6 | 0 | a02 | IIn | $M_{sh} = 6.0$ | 2.4 | 0 |
| z15D | CC | 15 | 1.2 | 0 | a03 | IIn | $M_{sh} = 10$ | 2.4 | 0 |
| z25D | CC | 25 | 1.2 | 0 | a04 | IIn | $M_{sh} = 20$ | 2.4 | 0 |
| z40D | CC | 40 | 1.2 | 0 | z15G | CC | 15 | 2.4 | 0 |
| z25G | CC | 25 | 2.4 | 0 | z40G | CC | 40 | 2.4 | 0 |

Table 1. Properties of CC (Whalen et al. 2013c), IIn (Whalen et al. 2013d) and PI SNe (Whalen et al. 2013a,b) explosions: progenitor mass (M_*), SN energy (E), and metallicity (Z). The Type IIn explosions all have a progenitor mass of $40 M_\odot$, but different shell masses and thus luminosities.

4 SYNTHETIC OBSERVATIONS

We generate synthetic LCs with a modified version of the *Super-Nova ANALYSIS* (SNANA; Kessler et al. 2009) LC simulator, as in DS13. It is a complete package for SN LC analysis, and accepts astrophysical characteristics of the source, IGM (see appendix A), and survey parameters as inputs. The SNe are specified by their source frame SEDs and \dot{n}_{SN} . The models simulated here span a wide range of progenitor parameters to emulate the diversity of SEDs expected in a real survey (Table 1). The probability of each SN is determined by the given IMF as described in Section 2.1. Other physical elements like IGM filtering and the primary reference star, which defines the magnitude system to be used, are convolved with the specific filter transmissions through the construction of k -correction tables. Such tables transform the fluxes from source frame to the observer frame, on top of which extinction by the Milky-Way is applied using full-sky dust maps (Schlegel et al. 1998)⁵. We also include telescope specifications such as CCD characteristics, field of view (FOV), point spread function (PSF) and pixel scale (Table D1). AB magnitudes are used for all the simulations presented here.

The instrument characteristics in our synthetic observations are based on NIRCam (appendix D; see also Gardner et al. 2006). All simulations assume individual integrations of 10^2 s, which can sometimes be co-added to create longer exposures.⁶ The two strategies tested here are the same as those in DS13 (Table 2):

Strategy 1 (str1) One pointing per year for each of the six reddest filters in NIRCam (F115W-F444W), to maximize our ability to identify high-redshift sources from non-detections in the bluest filters (dropouts).

Strategy 2 (str2) Three pointings per year separated by two-month gaps in filters F150W and F444W, to maximize the number of SN detections.

Both strategies assume a 5 yr survey time, with ~ 730 hours of telescope time per year and a sky coverage of 0.06 per cent.⁷ Finding at least a few detections near the LC peak is crucial to our goal of identifying these events as transients and photometrically categorizing them by SN type (e.g., Ishida & de Souza 2013). Therefore, for an event to be labelled a SN we require its detection at a minimum of one epoch before and after maximum brightness. We also require its detection at three epochs in at least one filter above the background limit and selection cuts on signal to noise (S/N) ratio ≥ 2 (cut1) and ≥ 3 (cut2) in at least one filter.

In Fig. 5, we show examples of LCs obtained by both strategies. The error bars denote the uncertainties in the magnitude measurements due to the background on the sky, photon statistics and instrument calibration. The errors are summed in quadrature and considered over an effective aperture based on PSF fitting, which we take to be Gaussian (see appendix C). From this figure, we con-

⁵ Our observation fields were centered around Hubble Ultra Deep Field (Beckwith et al. 2006).

⁶ Note that $\sim 10^3$ s is the limit for individual exposures due to cosmic ray contamination in the line of sight (Gardner et al. 2006).

⁷ NIRCam consists of two fully redundant optical trails, which allows simultaneous observations of the same FOV in 2 filters, one in lower (F070W-F200W) and the other in higher (F277W-F444W) wavelengths (Gardner et al. 2006). Taking advantage of this feature, our strategies were built so that each pointing gathers observations in 2 filters through 100s.

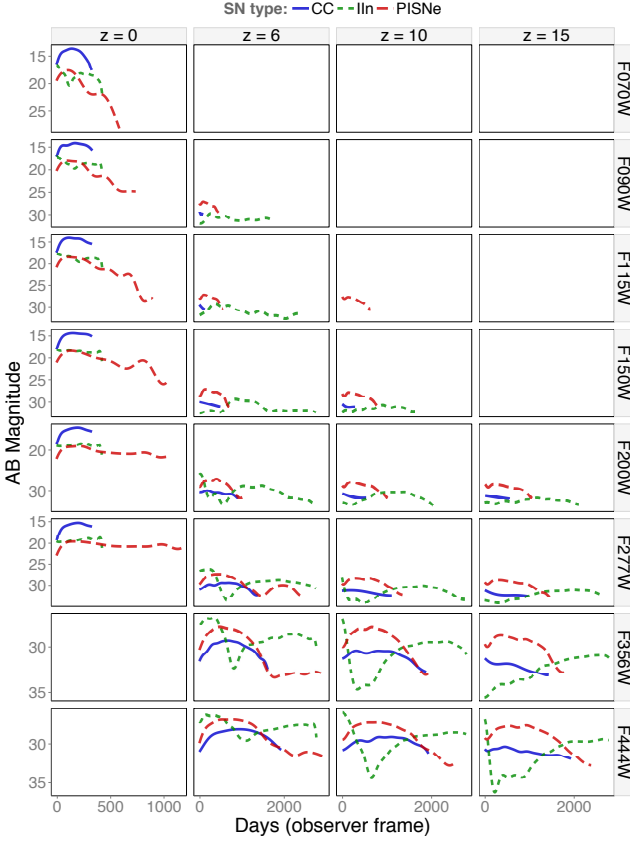


Figure 4. Light-curve evolution of the z40G CC SN (blue solid line), the a02 Type IIn (green dashed line), and the u200 PI SN (red long-dashed line). LCs are at $z = 0, 6, 10$ and 15 .

clude that detecting a SN in the six reddest filters indicates an event at moderate redshift, $z \lesssim 10$, while a detection in only the four reddest filters suggests a SN at $z \gtrsim 15$.

Fig. 6 shows the number of detections in comparison to the total number of SNe in the field. A few important conclusions can be drawn by inspecting the histograms:

- str2 clearly optimizes the detection rate of all SN types for cut1 for both SFR1 and SFR10 (using the same amount of time), but at the cost of getting information in a smaller number of filters. However, str1 seems to be more effective at detecting the higher quality LCs imposed by cut2. This is mainly due to the larger number of filters in this strategy, which increases the likelihood of finding a brighter event in at least one filter (the exact number of detections are presented later in Section 5 and Appendix B).
- The relative number of SNe detected of each type is strongly correlated with the underlying IMF, and therefore might be used as a probe of the Pop III IMF, as discussed later in this article. For instance, CC detections increase by almost an order of magnitude from the flat to the Salpeter IMF because the mass distribution of the latter is biased toward less massive stars.
- Given a fixed amount of telescope time, changing the observation strategy might increase the number of detections.

To be more quantitative, for the most optimistic case (SFR10+cut2) we obtain 39 ± 9 (67 ± 13) PI SNe, and 535 ± 33 (1451 ± 70) CC SNe with str1 (str2) for the Salpeter IMF. We find 76 ± 12 (124 ± 17) PI SNe and 61 ± 10 (159 ± 22) CC SNe with

str1 (str2) for the flat IMF. For Type IIn SNe, the detection rate is negligible, with ~ 1 event every 10 yr in the most optimistic case, so we do not bin them here.⁸ This is a clear indication that *JWST* can observe a large number of Pop III SNe, particularly CC SNe. Once potential candidates are detected, the brightest sources will be suitable for more detailed spectroscopic followup, which can place strong limits on their metal content.⁹

Whilst the PI SNe are brighter enough to be detected by *JWST* at redshifts as high as $z \sim 25$, the scarcity of such events makes their detection at the lowest redshifts more tangible. Our results are consistent with Hummel et al. (2012, Fig. 8) for an equivalent amount of time and FOV, although, some precaution must be taken when comparing numerical results. While they used a more stringent $10 - \sigma$ detection limit, they did not consider multiple observations in different filters, which demands a considerably amount of time. Nonetheless, similar to us, they conclude that the strategy more likely to succeed in detecting primordial SNe must rely on multiple field search strategy.

5 PROBING THE PRIMORDIAL IMF

The ultimate goal of a complete theory of primordial star formation is to predict the Pop III IMF from first principles (Bromm 2013). Finding the first cosmic explosions would be a leap forward in our understanding of the basic processes behind the formation of the first stars. Since each SN type to some degree encodes the mass of its progenitors, their relative rates can place firm constraints on the Pop III IMF.

But inferring the nature of a progenitor from its SN may not be simple. Even the progenitors of well-studied Type Ia SNe are not fully understood (Hillebrandt & Niemeyer 2000; Wang & Han 2012), although it is generally believed that they fall into one of two types: single-degenerate and double-degenerate mergers (Maoz et al. 2013). Techniques like integral field spectroscopy have been used to obtain both spatial and spectral information on the explosion site, allowing the identification of the parent population of the star. While many stellar evolution models have been proposed to characterize the progenitor stars, these predictions are still poorly supported by observations (Kuncarayakti et al. 2013). Given the aforementioned sources of uncertainties, instead of reconstructing the Pop III IMF directly from the data, we seek the answer to a more straightforward question: is it possible to distinguish a Salpeter IMF from a flat IMF by counting the relative observed rates of CC and PI SNe? In other words, we want to test the following null (\mathcal{H}_0) and alternative hypotheses (\mathcal{H}_a):

\mathcal{H}_0 : The relative observed frequencies of CC and PI SNe are independent of the IMF.

\mathcal{H}_a : The relative observed frequencies of CC and PI SNe are not independent of the IMF.

The CC and PI SNe can be treated as categorical variables,¹⁰ and their degree of dependence on the IMF can be investigated using the formalism of contingency tables (Becker et al. 1996). A 2×2 contingency table is a way of visualizing the dependence between

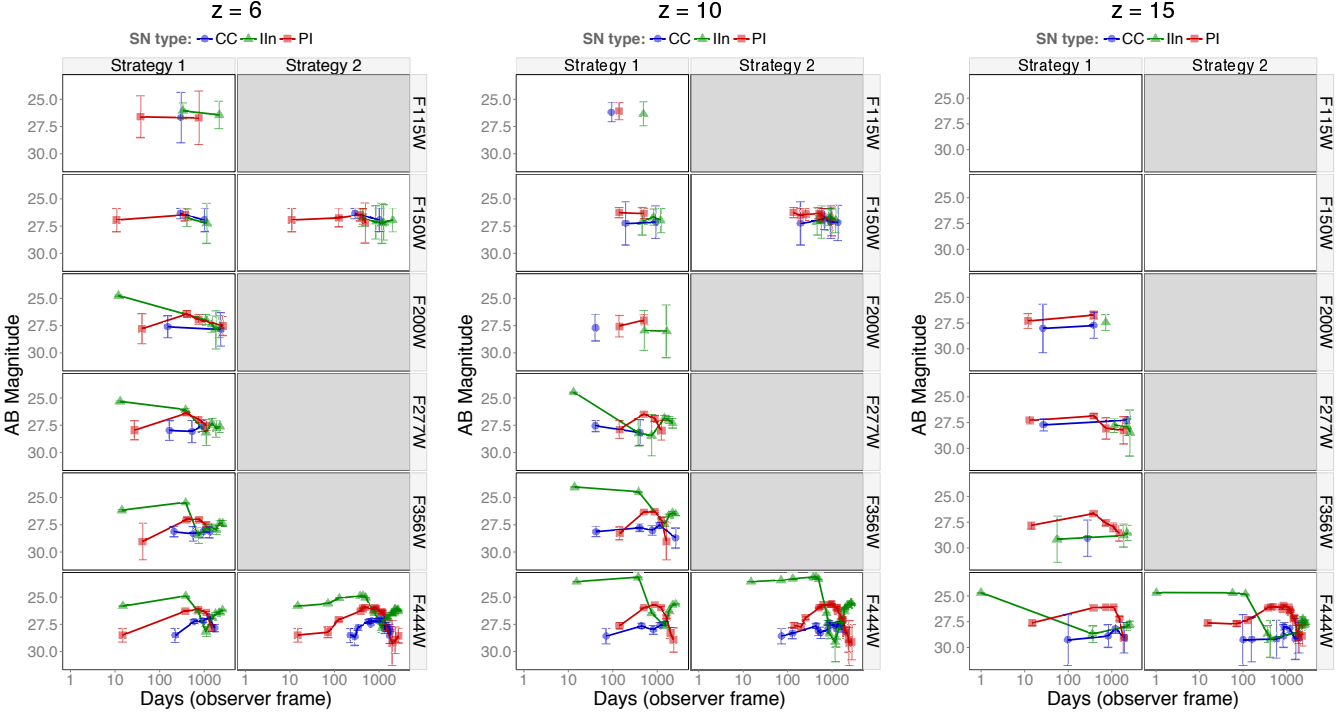
⁸ All numbers are an average over 200 simulations.

⁹ For low-metallicity objects, the ratio of oxygen lines to Balmer lines, such as [OIII]/H β , provides a linear measurement of metallicity.

¹⁰ Categorical data is composed of variables that can be separated into mutually exclusive classes, but there is no intrinsic ordering to the categories.

Table 2. Series of observational search strategies and selection cuts.

| Run | Sky (per cent) | Cadence | NIRCam Filters | <i>JWST</i> time per yr |
|----------------------------|---|--|----------------|-------------------------|
| Strategy 1 | 0.06 | One pointing per year | F115W-F444W | 730 h |
| Strategy 2 | 0.06 | Three pointings per year, two-month gaps | F150W, F444W | 730 h |
| Detectability requirements | | | | |
| Detection | At least one epoch before and one epoch after maximum | | | |
| | At least three epochs in one filter | | | |
| Minimum data quality | cut1: at least 1 filter with $S/N > 2$ | | | |
| | cut2: at least 1 filter with $S/N > 3$ | | | |

**Figure 5.** SEDs of CC, Type IIIn and PI SNe as they would be observed by the *JWST* NIRCam in our two observational strategies. We show each LC at $z = 6$ (left panel), 10 (central panel) and 15 (right panel). The y-axis is the observed magnitude and the x-axis is the time in the observer frame. The high-redshift events vanish from the bluest filters and their LCs last longer due to time dilation. The grey panels represent the filters not used by a specific strategy, and in the blank panels there were no detections.

two categorical variables (columns) and a given factor (rows). Examples of such tables for three of the scenarios in Fig. 6 are shown in Tables 3, 4 and 5. To measure the degree of correlation between them, we use the χ^2 test of independence.

Let O_{ij} be the original contingency table and E_{ij} be the one we would expect to measure if the categorical variables were independent. The latter is constructed by multiplying the sum of rows (R_i) and columns (C_j) of O_{ij} and then dividing by the total number of observations (N), $E_{ij} = R_i \times C_j / N$. In the tables described above, the E_{ij} for each case is shown in parentheses. We reject H_0 if the p -value¹¹ of the following χ^2 test is below a given signifi-

cance level α ,

$$\chi^2 = \sum_{i,j} \frac{(O_{ij} - E_{ij})^2}{E_{ij}}, \quad (2)$$

where typical values for α are 0.01 or 0.05, representing 99 and 95 per cent confidence levels, respectively. For instance, the χ^2 test for Table 3 is given by

$$\begin{aligned} \chi^2 &= \frac{(339 - 449.81)^2}{449.81} + \frac{(9312 - 9201.19)^2}{9201.19} \\ &+ \frac{(124 - 13.18995)^2}{13.18995} + \frac{(159 - 269.81)^2}{269.81} \approx 1005. \end{aligned} \quad (3)$$

In order to emulate a realistic scenario, we compared each of the synthetic observations with a basis model. Thus, the first row of all the tables are equal (representing our basis model) while the second row represents the observed sample for each case. Our fiducial model is composed of the total number of SNe expected to appear in the *JWST* survey area, assuming a Salpeter IMF and SFR10.

¹¹ p -value is the probability of obtaining a test statistic at least as extreme as the one that was actually observed, assuming that H_0 is true (e.g., Goodman 2008).

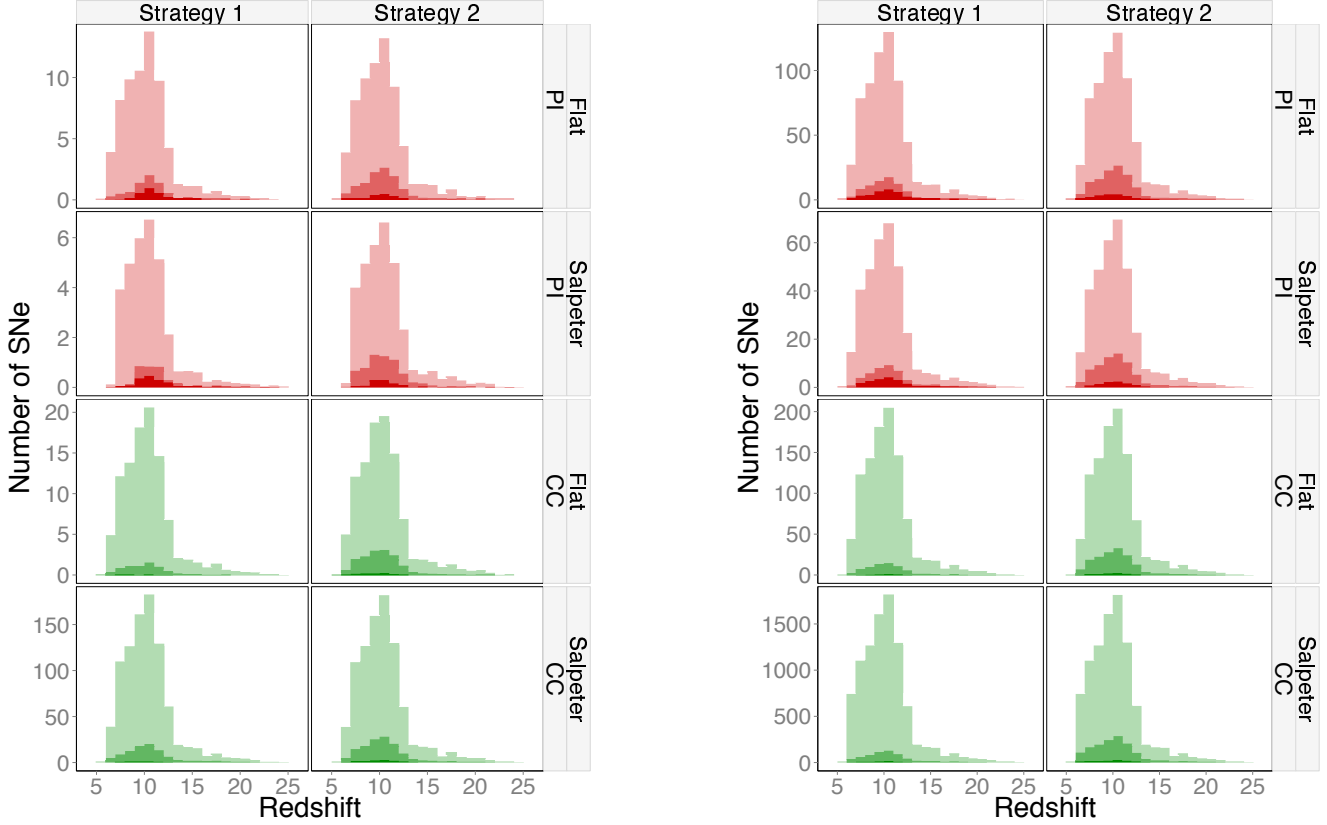


Figure 6. Number of total SN explosions during 5 yr mission in the observed field (lightest colours), and number of detected SNe after cut1 (middle colours) and cut2 (darkest colours) as a function of redshift for each model (CC, Type II and PI SNe), averaged over 200 realizations. Left panel: SFR1; right panel: SFR10. The left and right columns in each panel are for our two survey strategies, str1 and str2, and the rows indicate SN model and IMF. Note that not all axes are scaled the same.

Tables 3 and 4 show the contingency tables for observed samples with flat and Salpeter IMFs, respectively. Both tables assume SFR10 and cut1 (for the others, see appendix B). An observed sample whose IMF is flat is easily seen not to be Salpeter with a 99.95 per cent confidence level because $\chi^2 \approx 1005$, with a p -value $\lesssim 0.0005$. Furthermore, the observed sample whose IMF is Salpeter is not wrongly rejected due to observational bias, with $\chi^2 = 2.79$ and a p -value = 0.095. From Tables B1-B3, we see that the flat IMF is systematically rejected in all scenarios, showing high values of χ^2 : 365.5 (a p -value $\lesssim 0.0005$ for str2+cut2, 893.3 (a p -value $\lesssim 0.0005$) for str1+cut1, and 755.6 (a p -value $\lesssim 0.0005$) for str1+cut2.

In Tables B4-B6, we show the comparison with an observed sample generated from a Salpeter IMF. All values of χ^2 are lower than for the flat IMF, indicating a better agreement with \mathcal{H}_0 . Thus, we can already conclude that the χ^2 analysis is able to indicate the most likely IMF between two scenarios.

More insights can be gained from the relative risk (RR; Zhang & Yu 1998). If the samples are drawn from the same IMF, RR approaches 1, while it diverges from 1 when the samples are from two divergent IMFs. In other words, RR measures the probability of a certain event occurring in one group versus another. Therefore all numbers between brackets, representing the E_{ij} table, are constructed in such a way that $RR \approx 1$. Hence, our method determines if deviations from $RR = 1$ are driven by random fluctuations or by some intrinsic effect of the underlying IMF. An interesting effect arising from the RR analysis is the Malmquist bias,

which leads to the preferential detection of intrinsically brighter objects. Comparing Tables 4 and B4, the RR for PI SNe changes from 0.796 to 0.433 merely by changing the S/N requirement. This means that the probability of observing a PI SN is almost twice as high when cut2 is applied instead of cut1. This happens because the more stringent the detection limit, the more biased our sample will be towards brighter objects.

While the χ^2 analysis is useful for deciding which IMF better fits the data, it is also important for determining if the observed and theoretical samples are drawn from the same IMF in a self-consistent manner. For instance, because of the low number of events from str1, the p -value analysis *per se* wrongly rejects the Salpeter IMF, finding p -values < 0.05 (Tables B5 and B6). In other words, even if the fiducial and observed models are drawn from the same IMF, poor statistics may cause a bias in our conclusion. Thus, determining the proper size of a sample is a crucial step for experiment design, and it constitutes a branch in statistics known as power analysis that we discuss in greater detail below.

5.1 Sample size

Once we are convinced the above procedure is satisfactory for our purposes, we still need to optimize the use of telescope resources in order to design a realistic survey. Therefore, it is important to determine the minimum sample size necessary to measure a desired effect or to estimate how much should we trust a particular result, given the sample size allowed by observational constraints.

Otherwise, even if the survey is performed perfectly and analyzed properly, wrong conclusions could still be made due to the lack of statistical power (\mathcal{P}). \mathcal{P} can be understood to be the probability of rejecting \mathcal{H}_0 when \mathcal{H}_a is true. In our case, it represents the ability to detect true deviations from the Salpeter IMF in the observed sample. Therefore, while α represents the probability that \mathcal{H}_0 will be rejected when it is actually true (a wrong decision), \mathcal{P} quantifies the likelihood of rejecting \mathcal{H}_0 when it is actually false (a correct decision).

\mathcal{P} depends on the effect size (\mathcal{W}), confidence level, α , and number of detections, \mathcal{N} . \mathcal{W} determines the deviation from \mathcal{H}_0 that one would expect to detect. The number increases with the degree of discrepancy between the distribution of \mathcal{H}_a and \mathcal{H}_0 ,

$$\mathcal{W} = \sqrt{\sum_{i=1}^2 \frac{(P_{0i} - P_{Ei})^2}{P_{Ei}}}, \quad (4)$$

where P_{0i} and P_{Ei} are the proportions (counts divided by total number of observations) in each cell for the O_{ij} and E_{ij} contingency tables, respectively. It can be written in terms of χ^2 as $\mathcal{W} = \sqrt{\chi^2/\mathcal{N}}$. For our basis model shown in Table 5, $\mathcal{W} = 0.44$. Traditionally, $\mathcal{W} = 0.1, 0.3, 0.5$ are considered thresholds for small, medium and large differences, respectively (Cohen 1988). The χ^2 statistics follows a central χ_κ^2 distribution when \mathcal{H}_0 is true

$$\chi_\kappa^2(x) = \frac{x^{\kappa/2-1} e^{-x/2}}{\Gamma(\frac{1}{2}\kappa) 2^{\kappa/2}}, \quad (5)$$

where Γ is the gamma function (e.g., Abramowitz & Stegun 1965) and κ stands for degrees of freedom (equal to one for 2×2 tables). While it follows a noncentral $\chi_\kappa^2(\lambda)$ distribution if \mathcal{H}_0 is false,

$$\chi_\kappa^2(x, \lambda) = \frac{e^{-(x+\lambda)/2} x^{(\kappa-1)/2} \sqrt{\lambda}}{2(\lambda x)^{\kappa/4}} I_{\kappa/2-1}(\sqrt{\lambda x}), \quad (6)$$

where $I_n(x)$ is the modified Bessel function of the first kind (e.g., Abramowitz & Stegun 1965). \mathcal{P} represents our ability to discriminate between χ_κ^2 and $\chi_\kappa^2(\lambda)$ at a certain α ,

$$\mathcal{P} = P(\chi_\kappa^2(x, \lambda) \geq \chi_{\kappa; 1-\alpha}^2(x)), \quad (7)$$

where $\lambda = \mathcal{W}\mathcal{N}$ is the noncentrality parameter. If both samples are equal, \mathcal{H}_0 is true and $\mathcal{W} = \lambda = 0$. Hereafter, all calculations are performed with $\alpha = 0.05$ or at 99.5 per cent confidence level.

In Fig. 7 we show a graphical representation of \mathcal{P} . The shaded red area on the left of the grey-dashed line at $\chi^2 = 3.84$ represents 99.5 per cent confidence level for the χ_κ^2 . In this context, \mathcal{P} is the area under $\chi_\kappa^2(\lambda)$ falling on the right side of the grey-dashed line. Therefore the rightmost the $\chi_\kappa^2(\lambda)$ distribution for \mathcal{H}_a is, the easier it will be to discriminate it from the χ_κ^2 distribution. Higher values of λ implies higher deviations from χ_κ^2 . Hence, \mathcal{P} grows in the same way as the number of detections.

In Fig. 8 we show that $\sim 10^2$ SN detections are necessary to distinguish between a Salpeter and a flat IMF with the χ^2 test. It is important to note that the former number represents the number of SNe properly classified within their respective categories, not the total number of SNe appearing in the FOV. This is a remarkable result because it shows that the Pop III IMF could be unveiled in the near future given a reasonable amount of telescope time.

Finally, the methodology suggested here is broad enough to determine which of two IMF better describe the data. We use the Salpeter and flat IMF as a benchmark of the test since these are

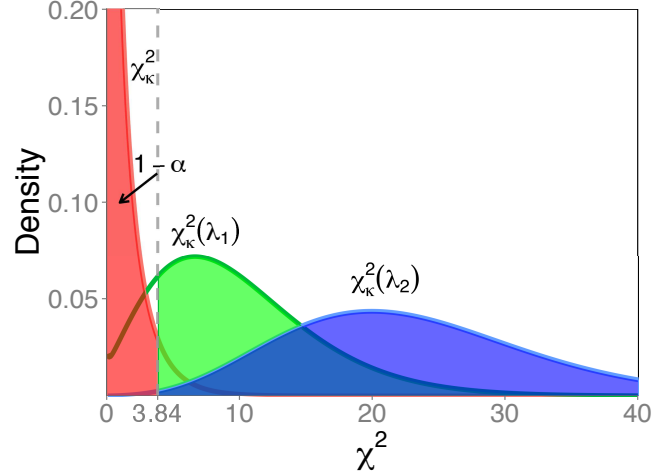


Figure 7. The red curve denotes the χ_κ^2 distribution under \mathcal{H}_0 . The blue and green curves are the distribution under \mathcal{H}_a for noncentrality parameter $\lambda_1 = 20 \times 0.44$ (20 detections, $\mathcal{W} = 0.44$) and $\lambda_2 = 50 \times 0.44$ (50 detections, $\mathcal{W} = 0.44$) respectively. The vertical dotted grey line represents the χ^2 value with a probability of 0.05 under \mathcal{H}_0 . If we get a χ^2 statistic to the left of the line we conclude that it came from the \mathcal{H}_0 and if it is to the right of the line then we conclude it came from \mathcal{H}_a . The area under the alternative distribution to the right of the line represents the power of the test. Thus, the higher the number of observations, more straightforward is to discriminate \mathcal{H}_a from \mathcal{H}_0 . Which in our case represents the ability to conclude if the distribution is consistent with Salpeter or not.

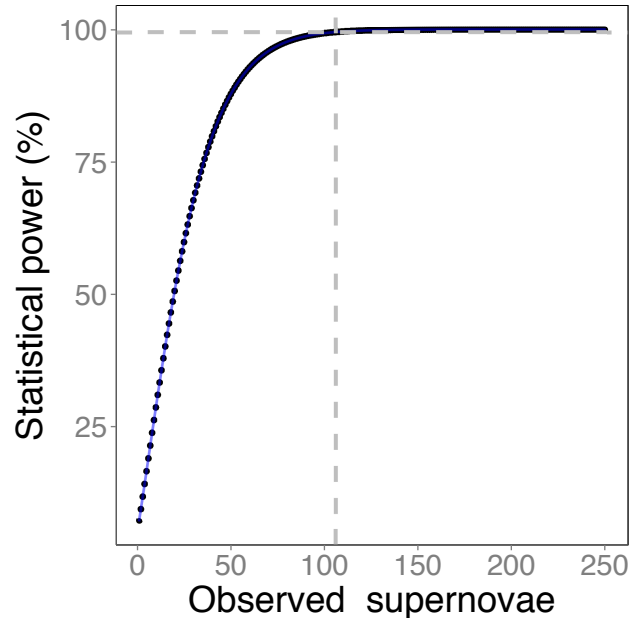


Figure 8. Power estimation as a function of the number of detected SN, demonstrating that to achieve a power of 99.5% (horizontal dashed gray line), it is necessary to detect at least 105 SNe (vertical dashed gray line).

two physically motivated models. Furthermore our methodology defines a straightforward way to determine the minimum sample requirements to achieve a reliable result.

Table 3. Contingency table for the fiducial model and the case with flat IMF, SFR10, cut1 and str2.

| IMF | SN type | | Total by IMF |
|-----------------------------|--------------|----------------|--------------|
| | PI SN | CC | |
| Salpeter _(all) | 339 (449.81) | 9312 (9201.19) | 9651 |
| Flat _(cut1;str2) | 124 (13.19) | 159 (269.81) | 283 |
| Total by type | 463 | 9471 | 9934 |

- Relative risk: PI SN = $\frac{339/9651}{124/283} \approx 0.080$ CC = $\frac{9312/9651}{159/283} \approx 1.717$
- $\chi^2 = 1005.068$ p-value < 0.0005

Table 4. Contingency table for the fiducial model and the case with Salpeter IMF, SFR10, cut1 and str2.

| IMF | SN type | | Total by IMF |
|---------------------------------|--------------|----------------|--------------|
| | PI SN | CC | |
| Salpeter _(all) | 339 (350.82) | 9312 (9300.18) | 9651 |
| Salpeter _(cut1;str2) | 67 (55.18) | 1451 (1462.82) | 1518 |
| Total by type | 406 | 10763 | 11169 |

- Relative risk: PI SN = $\frac{339/9651}{67/1518} \approx 0.796$ CC = $\frac{9312/9651}{1451/1518} \approx 1.009$
- $\chi^2 = 2.79$ p-value = 0.095

6 SUPERNOVA TYPING

The analysis delineated in the last section implicitly assumes that all SNe have been properly classified into their own groups. Nevertheless, once we have identified a Pop III SNe, we must classify them into PISN/CC events and provide some estimate of the level of contamination. These are far from trivial tasks and a detailed study of all nuances underlying the SNe photometric classification (Ishida & de Souza 2013) demands a separate work. However, we describe below how such problems can be tackled, demonstrating once more the potential of Pop III synthetic surveys as test grounds for future analysis.

Distinguishing between PI and CC SNe would be fairly straightforward if one can measure their redshift. In rest-frame, NIR PISN light curves last significantly longer than CC ones due to longer radiation diffusion timescales in their more massive ejecta. Although, before performing a time consuming spectroscopic follow-up on such faint targets, it is wise to develop an optimized strategy for photometric classification to identify potential candidates. This subject is already highly developed within the type Ia SN community (Kessler et al. 2010), and the existing approaches are usually divided in two classes: empirical (e.g., Newling et al. 2011; Richards et al. 2012; Karpenka et al. 2012; Ishida & de Souza 2013) and template fitting (e.g., Sullivan et al. 2006; Poznanski et al. 2007; Kuznetsova & Connolly 2007; Kunz et al. 2007; Sako et al. 2008;

Table 5. Contingency table for the total number of SNe expected to appear in the JWST survey area for the fiducial model and the case with a flat IMF.

| IMF | SN type | | Total by IMF |
|---------------------------|--------------|----------------|--------------|
| | PI SN | CC | |
| Salpeter _(all) | 339 (834.57) | 9312 (8816.43) | 9651 |
| Flat _(all) | 638 (142.43) | 1009 (1504.58) | 1647 |
| Total by type | 977 | 10321 | 11298 |

- Relative risk: PI SN = $\frac{339/9651}{638/1647} \approx 0.091$ CC = $\frac{9312/9651}{1009/1647} \approx 1.575$
- $\chi^2 = 2209.739$ p-value < 0.0005

Rodney & Tonry 2009; Sako et al. 2011) methods. The former uses magnitudes and/or fluxes of a spectroscopically measured sample for training the method, which is then applied to the photometric sample. The latter, try to find spectral template and redshift which best fit the photometric observations using a library of well know observational or synthetic spectra.

Since we have not yet observed any Pop III stars, which could in principle be used as a training sample, the best we can do is to base our analysis on synthetic LCs in order to estimate our potential power in discriminating between CC and PI SNe. Following the procedure suggested by Ishida & de Souza (2013, see appendix E1), we present in Fig. 9 the projections of CC and PISN LCs into a 2-dimensional space obtained from Kernel Principal Component Analysis (KPCA). Each point represents a LC observed in filters F200W, F277W, F356W and F444W with a cadence of two months in each filter. The dispersion of the projected points are mainly caused by the intrinsic variance of different SN models, S/N and redshift. Each SN type in the figure is identified by colour, while the marker style indicates if an object was correctly classified or not by a cross-validation procedure using the *k*-nearest neighbor predictor within a *Leave One Out* (LOO) cross-validation procedure (appendix E3).

In the context of this work, each iteration of the LOO algorithm can be interpreted as an attempt to classify a new unknown object given the synthetic data set. Consequently, the cross-validation can be understood as an indicative of the power of the method in discriminating between each class of SN. Nevertheless a more realistic prediction requires the application of the trained classifier to a new set of LCs whose classes are unknown. Furthermore, we should carry an exhaustive study of the observational cadency, data quality, expected amount of spectroscopic confirmed and photometric objects of each type, LC fitting method, number of used photometric bands, and so on (Ishida & de Souza 2013). Such analysis is out of the scope of the present work, but planned to be carried in the future.

The confusion matrix for the objects present in Fig. 9 is given in Table 6, representing the number of SN correctly (diagonal) and incorrectly (off-diagonal) classified during the cross-validation. For this example case, the method achieve an accuracy of ~ 76.3 per cent. Assuming that the real SN will not be very different from our simulations, the results suggests an approximate upper limit for our ability to correctly discriminate between these objects. It has direct implications in the analysis developed in Section 5.1, which implicitly assumes an error-free classification of the LCs.

In other words, standard power analysis does not take into account the reliability (\mathcal{R}) of the measurement. According to (Kanyongo et al. 2007), a $\mathcal{R} \neq 1$ affects \mathcal{P} by indirectly changing \mathcal{W} as follows

$$\mathcal{W}_{obs} = \mathcal{W}\sqrt{\mathcal{R}}, \quad (8)$$

where \mathcal{R} is defined by the ratio of true variance (σ_{true}^2) to observed variance (σ_{obs}^2)

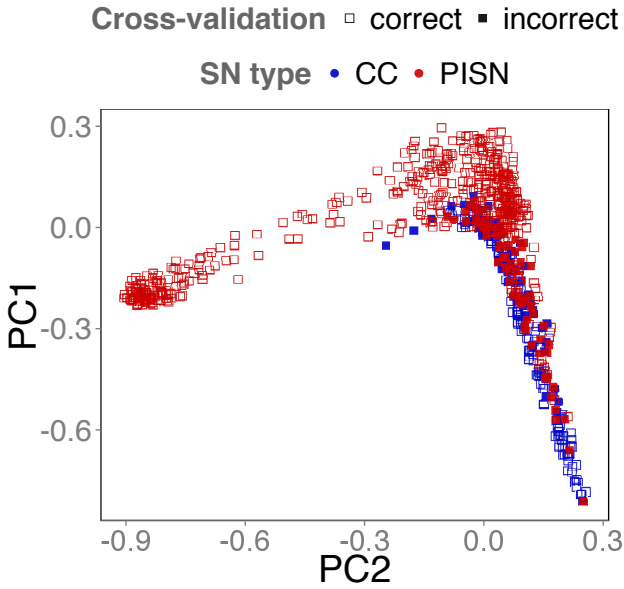
$$\mathcal{R} = \frac{\sigma_{true}^2}{\sigma_{obs}^2}. \quad (9)$$

By changing \mathcal{W} , we increase the number of observed objects necessary to reach the same \mathcal{P} . For instance, considering $\mathcal{R} = 0.7$ (0.6) would increase the number of objects necessary to reach a power of 99.5 per cent to ~ 150 (180) SN. Therefore considering a feasible

Table 6. Confusion Matrix.

| Predicted | Observed | |
|-----------|----------|-------|
| | CC | PI SN |
| CC | 302 | 129 |
| PI SN | 144 | 576 |

- Number of correct classifications: $302+576 = 878$
- Number of incorrect classifications: $129+144 = 273$
- Accuracy: $878/(878+273) \approx 0.763$

**Figure 9.** Kernel Principal Components projection of the LCs from CC (blue symbols) and PI (red symbols). Empty square represents SN correctly classified and filled square SN wrongly classified by the cross-validation using k -nearest neighbourhood algorithm.

level of purity in our data would demand $\lesssim 2 \times 10^2$ high redshift SN to discriminate between a primordial Salpeter or flat IMF.

An issue still remains, even if we are able to discriminate between a Pop III CC and a PI SN, we still need to distinguish between a Pop II from Pop III SN. For instance, CC SN in both populations have similar energies and line spectra due to internal mixing and fallback prior to shock breakout from the surface of the star. Therefore, to be certain we are probing the Pop III IMF and not the total one, we should observe SN in redshifts as high as $z \gtrsim 12$. In Fig. 10 we show the average number of detection of each type above a given redshift over 5 yrs of JWST mission. Using $\lesssim 10$ per cent of JWST time allow us to reach the minimum number to probe the IMF in few scenarios, but not all. However JWST has fuel for a 10 yrs mission, which considerably improves the possibility of achieving such goal, but only if a well planed and dedicated strategy is implemented. While the Pop III/Pop II identification has no effect in our power analysis, it implies that, due to a high level of contamination, it might only be possible to probe the total IMF instead of the primordial one.

7 CONCLUSIONS

We have created the first, detailed synthetic observations of Pop III SNe. With cosmological and radiation hydrodynamics simulations, together with detailed models of instrument properties and IGM absorption, we show that a viable survey strategy could detect up to ~ 300 CC and ~ 15 PI SNe per year. We also find that information from multiple filters is crucial for detecting and distinguishing high- z SN candidates from low- z events with dropout techniques. Our study also shows that the low rates of Type II SN will likely prevent their detection in deep-field surveys, and all-sky missions such as *Euclid* will be better suited for this task. Survey strategies for Pop III SN in all-sky missions such as *Euclid*, *WFIRST* and *WISH* will be examined in future work.

New calculations now show that additional SN types not considered here will also be visible at high redshifts. Whalen et al. (2013f) have now shown that $100 - 140 M_{\odot}$ PPI SNe will be visible to *JWST* at $z \sim 10 - 20$, and, depending on the Pop III IMF, may be as numerous as PI SNe (see also Woosley et al. 2007). Hypernovae, the highly energetic and asymmetric explosions of $40 - 60 M_{\odot}$ stars, will likewise be visible out to $z \sim 10 - 15$ (Smidt et al. 2013), and detection limits in redshift for $85 - 135 M_{\odot}$ PI SNe are now being investigated (Whalen et al. 2013g). These additional SN classes will be considered in future mock surveys.

Our synthetic survey allows us to perform the first comprehensive statistical study on the feasibility of using the first cosmic explosions to constrain the Pop III IMF by counting the relative detection rates of CC and PI SNe. Given the realism with which we simulate the observing process, our synthetic sample may be easily used to calibrate photometric classification techniques. Using the formalism of contingency tables together with well-established χ^2 statistics, we show that at least $\sim 10^2$ SNe detections will be necessary to distinguish between Salpeter and flat IMFs with a 99.5 per cent confidence level. We show that ML techniques constitute a promising tool to discriminate between Pop III SNe only relying on photometric information. Even if the accuracy of our classification is as low as 60 per cent, we show that $\lesssim 200$ observations are enough to discriminate between the two IMFs. This represents a leap forward in high-redshift SN studies, which will shed light on the long-standing puzzle of the primordial IMF.

ACKNOWLEDGMENTS

DJW acknowledges support from the Baden-Württemberg-Stiftung by contract research via the programme Internationale Spitzenforschung II (grant P- LS-SPII/18). EEOI thanks the Brazilian agencies FAPESP (2011/09525-3) and CAPES (9229-13-2) for financial support. Work at LANL was done under the auspices of the National Nuclear Security Administration of the US Department of Energy at Los Alamos National Laboratory under Contract No. DE-AC52-06NA25396. We thank Joseph Smidt for providing part of the data present in Fig. 1. RSS thanks MPA for the hospitality during the preparation of this work.

APPENDIX A: IGM ABSORPTION

The spectra of events at $z > 6$ blueward of $1216(1+z)\text{\AA}$ (Gunn & Peterson 1965; Mesinger et al. 2004) are heavily ab-

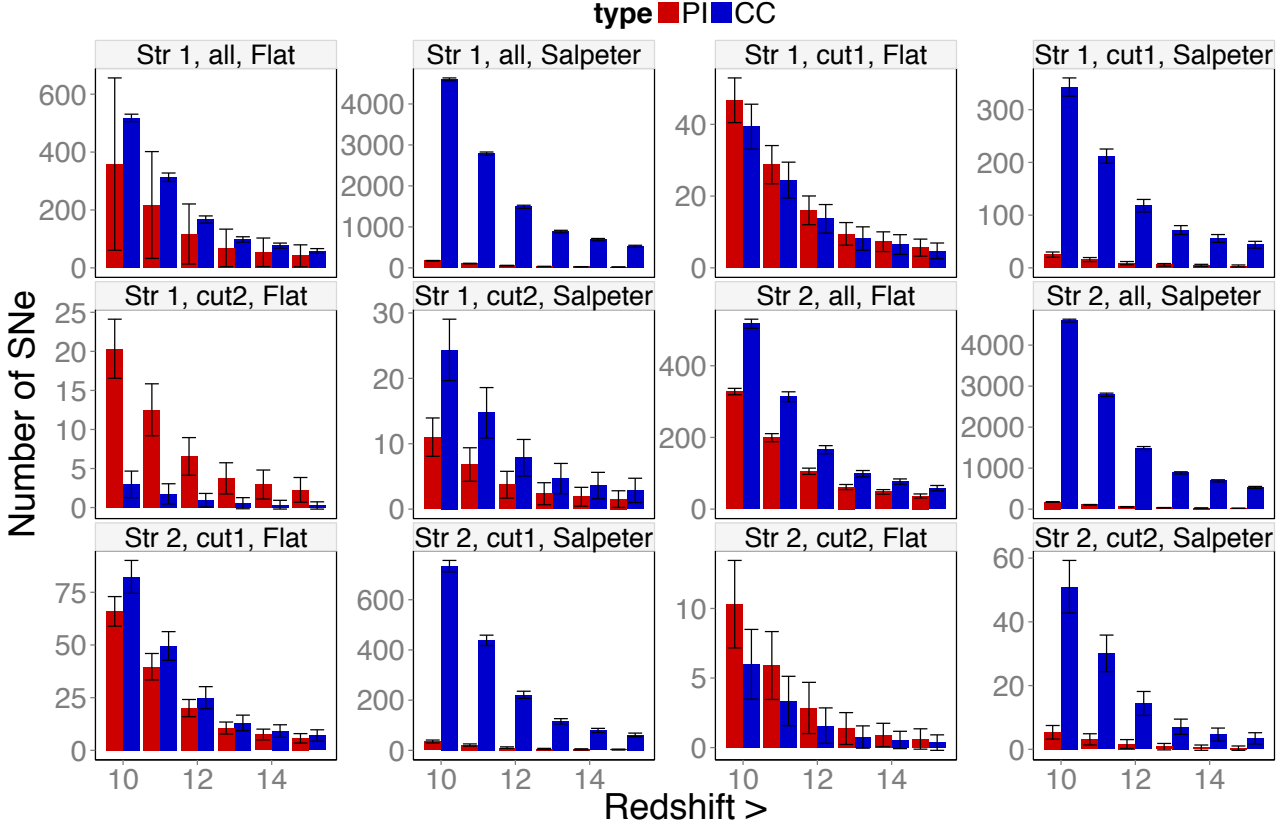


Figure 10. Number of SNe detections above a certain redshift. Each column represents an average value over 200 realizations for PI (red bar) and CC (blue bar) SN detections. The standard deviation around the mean is given by the error bars.

sorbed by the neutral IGM (Ciardi et al. 2012).¹² The contribution to the optical depth τ_{IGM} comes mainly from damped Ly α absorbers (DLAs), Lyman Limit Systems (LLSs), optically thin systems and resonance line scattering by the Ly α forest along the line of sight. We account for absorption by the neutral IGM at high- z by multiplying each SED by the IGM transmission function for the source redshift. The observed spectrum ($f_{\lambda, \text{obs}}$) after IGM attenuation is

$$f_{\lambda, \text{obs}} = f_{\lambda} e^{-\tau_{\text{IGM}}}. \quad (\text{A1})$$

We compute transmission through the IGM with the JAVA code IGMTRANSMISSION (Harrison et al. 2011). Our model uses a Monte-Carlo approach to distribute LLSs chosen from a redshift distribution (dN/dz) and an optical depth distribution ($dN/d\tau_L$), averaged over IGM transmission along many lines of sight (Meiksin 2006).

The contribution from optically thin systems is

$$\tau_L^{\text{IGM}} = 0.07553(1+z_L)^{4.4} \left[\frac{1}{(1+z_L)^{\frac{3}{2}}} - \frac{1}{(1+z)^{\frac{3}{2}}} \right], \quad (\text{A2})$$

where $z_L = \lambda/\lambda_L - 1$ and $\lambda_L = 912 \text{ \AA}$. The contribution due to

the optically thick ($\tau_L > 1$) LLSs is

$$\tau_L^{\text{LLS}} = \int_{z_L}^z dz' \int_1^{\infty} d\tau_L \frac{\partial^2 N}{\partial \tau_L \partial z'} \left\{ 1 - \exp \left[-\tau_L \left(\frac{1+z_L}{1+z'} \right)^3 \right] \right\}, \quad (\text{A3})$$

where $\frac{\partial^2 N}{\partial \tau_L \partial z'}$ is the number of absorbers along the line of sight per unit redshift interval per unit optical depth of the system.

The spatial distribution of the LLSs is (Meiksin 2006)

$$\frac{dN}{dz} = N_0(1+z)^{\gamma}, \quad (\text{A4})$$

where $N_0 = 0.25$ and $\gamma = 1.5$. The optical depth distribution is

$$\frac{dN}{d\tau_L} \propto \tau_L^{-\beta}, \quad (\text{A5})$$

where $\beta = 1.5$.

APPENDIX B: CONTINGENCY TABLES

Contingency tables are used to analyse the relationship between two or more categorical variables. It is the categorical equivalent of the scatter plot used to analyse the relationship between two continuous variables. A categorical variable is one that has two or more classes, but there is no intrinsic ordering between them. For example, gender is a categorical variable having two possible classes (male and female), and there is no intrinsic ordering to the categories. Hence, the SN types can be treated as categorical variables since they are mutually exclusive.

¹² In principle, the IGM can also absorb photons redward of $1216(1+z) \text{ \AA}$ by the Ly α damping wing cross-section (Miralda-Escude 1998; Mesinger & Furlanetto 2008; Bolton & Haehnelt 2013). This serves to lessen the discontinuity in τ at $1216(1+z) \text{ \AA}$, but does not affect our conclusions.

Table B1. Contingency table for the fiducial model and the case with a flat IMF, SFR10, cut2 and str2.

| IMF | SN type | | Total by IMF |
|-----------------------------|--------------|----------------|--------------|
| | PI SN | CC | |
| Salpeter _(all) | 339 (359.77) | 9312 (9291.23) | 9651 |
| Flat _(cut2;str2) | 22 (1.23) | 11 (31.77) | 33 |
| Total by type | 361 | 9323 | 9684 |

- Relative risk: $\text{PI SN} = \frac{339/9651}{22/33} \approx 0.053$ $\text{CC} = \frac{9312/9651}{11/33} \approx 2.894$
- $\chi^2 = 365.5$ p-value < 0.0005

Table B2. Contingency table for the fiducial model and the case with a flat IMF, SFR10, cut2 and str1.

| IMF | SN type | | Total by IMF |
|-----------------------------|--------------|----------------|--------------|
| | PI SN | CC | |
| Salpeter _(all) | 339 (409.19) | 9312 (9241.81) | 9651 |
| Flat _(cut1;str1) | 76 (5.80) | 61 (131.19) | 137 |
| Total by type | 415 | 9373 | 9788 |

- Relative risk: $\text{PI SN} = \frac{339/9651}{76/137} \approx 0.063$ $\text{CC} = \frac{9312/9651}{61/137} \approx 2.167$
- $\chi^2 = 898.3$ p-value < 0.0005

We can measure the association between the occurrence of a CC or PI SN and the IMF through their RR. In Table B1, we have an example of RR calculation for the fiducial model and the case with a flat IMF, SFR10, cut2 and str2. The RR in this case is 2.894 for CC SNe and 0.053 for PI SNe, meaning that a Salpeter IMF is ~ 3 times more likely to produce a CC event than in the flat IMF.

APPENDIX C: NOISE CALCULATION

This section briefly describes how the uncertainties in measured fluxes and magnitudes are built (error bars in Fig. 5). A more in-depth discussion and example calculation can be found in the SNANA Manual,¹³ section 4.12.

Consider the simulation of the observation of an event in a filter at one epoch. The SED describes the evolution of the spectrum of this event over time in the frame of the SN. This information is then redshifted into the observer frame, taking into account cosmological dimming, absorption by the IGM, Milky Way extinction, the collection area of the telescope mirror, total exposure time, etc. The product of this calculation is the AB magnitude (m) of the SN, minus the errors due to the observing process. In order to evaluate

¹³ http://sdssdp62.fnal.gov/sdssn/SNANA-PUBLIC/doc/snana_manual.pdf

Table B3. Contingency table for the fiducial model and the case with a flat IMF, SFR10, cut2, and str1.

| IMF | SN type | | Total by IMF |
|-----------------------------|--------------|----------------|--------------|
| | PI SN | CC | |
| Salpeter _(all) | 339 (371.54) | 9312 (9279.46) | 9651 |
| Flat _(cut2;str1) | 34 (1.46) | 4 (36.54) | 38 |
| Total by type | 373 | 9316 | 9689 |

- Relative risk: $\text{PI SN} = \frac{339/9651}{34/38} \approx 0.039$ $\text{CC} = \frac{9312/9651}{4/38} \approx 9.166$
- $\chi^2 = 755.6$ p-value < 0.0005

Table B4. Contingency table for the fiducial model and the case with a Salpeter IMF, SFR10, cut2, and str2.

| IMF | SN type | | Total by IMF |
|---------------------------------|--------------|----------------|--------------|
| | PI SN | CC | |
| Salpeter _(all) | 339 (344.04) | 9312 (9306.96) | 9651 |
| Salpeter _(cut2;str2) | 9 (3.96) | 102 (107.04) | 111 |
| Total by type | 348 | 9414 | 9762 |

- Relative risk: $\text{PI SN} = \frac{339/9651}{9/111} \approx 0.433$ $\text{CC} = \frac{9312/9651}{102/111} \approx 1.050$
- $\chi^2 = 6.74$ p-value = 0.02

Table B5. Contingency table for the fiducial model and the case with a Salpeter IMF, SFR10, cut1, and str1.

| IMF | SN type | | Total by IMF |
|---------------------------------|--------------|----------------|--------------|
| | PI SN | CC | |
| Salpeter _(all) | 339 (356.78) | 9312 (9294.22) | 9651 |
| Salpeter _(cut1;str1) | 39 (21.22) | 535 (552.78) | 574 |
| Total by type | 378 | 9847 | 10225 |

- Relative risk: $\text{PI SN} = \frac{339/9651}{39/574} \approx 0.517$ $\text{CC} = \frac{9312/9651}{535/574} \approx 1.035$
- $\chi^2 = 16.39$ p-value = 0.0005

these errors and account for them into our synthetic observations, we need to incorporate at least 3 important sources of uncertainty:

- the determination of the signal itself, σ_{sig} ;
- sky background, σ_{sky} ;
- calibration process (determination of the zero point), σ_{ZPT} .

The measured source signal can be expressed in terms of the number of photoelectrons generated in the CCD, N_{pe} . In this case, $\sigma_{\text{sig}} = G^{-1} \sqrt{N_{\text{pe}}}$ in analog-to-digital-units (ADU), where G is the CCD gain (pe/ADU). The sky background error is given by $\sigma_{\text{sky}} = \pm \sqrt{A \sigma_{\text{skypix}}^2}$, where A is the PSF equivalent area, represented by a simple Gaussian of full-width-at-half-maximum σ_1 ($A = 4\pi\sigma_1^2$), and σ_{skypix} is the measured uncertainty in sky brightness per pixel (ADU/pixel). The error coming from the zero point magnitude (σ_{ZPT}) encodes information about the atmospheric transparency and telescope aperture and efficiency, but does not depend on the signal from this particular object. Thus, the statistical error due to photon statistics is composed of σ_{sig}/F and σ_{sky}/F . These should be added in quadrature to σ_{ZPT} , which represents an additional statistical error coming from stellar calibration.

Finally, the uncertainty in flux determination (in ADU) is

Table B6. Contingency table for the fiducial model and the case with a Salpeter IMF, SFR10, cut2, and str1.

| IMF | SN type | | Total by IMF |
|---------------------------------|--------------|----------------|--------------|
| | PI SN | CC | |
| Salpeter _(all) | 339 (354.01) | 9312 (9296.98) | 9651 |
| Salpeter _(cut2;str1) | 17 (1.98) | 37 (52.01) | 54 |
| Total by type | 356 | 9349 | 9705 |

- Relative risk: $\text{PI SN} = \frac{339/9651}{17/54} \approx 0.112$ $\text{CC} = \frac{9312/9651}{37/54} \approx 1.408$
- $\chi^2 = 118.9$ p-value = 0.0005

Table D1. *JWST* technical specifications used to construct the simulation library. ZPTSIG: additional smearing to zero; full-width-at-half-maximum (FWHM), NIRCam field of view (FOV), mirror collecting area (A), pixel scale and CCD gain/noise (Gardner et al. 2006, and references therein).

| Feature | value |
|-----------------------------------|--|
| CCD gain (e ⁻ /ADU) | 3.5 |
| CCD noise (e ⁻ /pixel) | 4.41 |
| Pixel scale (arcsec/pixel) | 0.032 for F070W-F200W 0.065 for F277W-F444W |
| FWHM (pixels) | 2 |
| σ_{ZPT} | 0.004 |
| FOV (arcmin ²) | 9.68 |
| A (cm ²) | 2.5×10^5 |

Table D2. Inputs used in the construction of the SNANA simulation library (SIMLIB) file for *JWST*. Columns correspond to NIRCam filter, zero point for AB magnitudes (m_{ZPT}), sky brightness (m_{sky}) and error in sky brightness (σ_{sky}). All values were calculated for an exposure time of 10^3 s.

| NIRCam filter | m_{ZPT} (mag/arcsec ²) | m_{sky} (mag/arcsec ²) | σ_{sky} (ADU/pixel) |
|---------------|--|--|--------------------------------------|
| F070W | 27.87 | 27.08 | 1.24 |
| F090W | 28.41 | 26.90 | 1.34 |
| F115W | 28.89 | 26.76 | 1.39 |
| F150W | 29.51 | 26.88 | 1.35 |
| F200W | 30.20 | 26.96 | 1.34 |
| F277W | 30.85 | 26.32 | 1.75 |
| F356W | 31.38 | 26.75 | 1.43 |
| F444W | 31.88 | 25.58 | 2.47 |

given by

$$\sigma_F = F \times \sqrt{\frac{(\sigma_{\text{sig}}^2 + \sigma_{\text{sky}}^2)}{F^2} + \sigma_{\text{ZPT}}^2}, \quad (\text{C1})$$

where $F = 10^{-0.4(m - m_{\text{ZPT}})}$ is the flux from the source, m is its corresponding magnitude, and m_{ZPT} is the zero point magnitude. To calculate the error in m , we define

$$\sigma_{m\pm} = -5 \log_{10} \left(\frac{F}{F \pm \sigma_F} \right). \quad (\text{C2})$$

This equation is used to determine right and left limits for the case of asymmetric errors. In the simple case where the confidence levels in magnitude are symmetric, the observed error is defined as

$$\sigma_m = \frac{|\sigma_{m+}| + |\sigma_{m-}|}{2}. \quad (\text{C3})$$

APPENDIX D: JWST SPECIFICATIONS

To account for instrument characteristics, we use specifications from NIRCam and other sources shown in Table D1. For completeness, we also show explicit values for the zero point, sky magnitude and error in sky magnitudes for each filter in Table D2. The CCD readout noise and sky-noise are determined by the CDD-noise and σ_{sky} parameters summed in quadrature over A based on the PSF fitting.

APPENDIX E: SUPERNOVA PHOTOMETRIC CLASSIFICATION

E1 Kernel Principal Components Analysis

KPCA generalizes the standard PCA by first mapping the data into a higher dimensional feature space \mathbb{F} :

$$\begin{aligned} \Phi : \mathbb{R}^n &\rightarrow \mathbb{F} \\ \mathbf{x} &\rightarrow \Phi(\mathbf{x}), \end{aligned} \quad (\text{E1})$$

where Φ is a nonlinear function and \mathbb{F} has arbitrary number of dimensions.

The covariance matrix, $C_F \in \mathbb{F}$, will be defined similarly as

$$C_F = \frac{1}{N} \sum_{i=1}^N \Phi(x_i) \Phi(x_i)^T. \quad (\text{E2})$$

We assume that $\Phi(\mathbf{x}_i)$ are centered in feature space. Consider \mathbf{v}_Φ^l the l -th eigenvector of C_F and λ_Φ^l its l -th eigenvalue. We can define a kernel $N \times N$ matrix

$$K_F(\mathbf{x}_i, \mathbf{x}_j) = (\Phi(\mathbf{x}_i) \cdot \Phi(\mathbf{x}_j)), \quad (\text{E3})$$

which allows us to compute the value of dot product in \mathbb{F} without carrying out the map Φ . The kernel function has to satisfy the Mercer's theorem to ensure that it is possible to construct a mapping into a space where K_F acts as a dot product. The projection of a new test point, \mathbf{n} , is given by

$$(\mathbf{v}_\Phi^l \cdot \Phi(\mathbf{n})) = \sum_{i=1}^N \alpha_{\Phi_i}^l K_F(\mathbf{x}_i, \mathbf{n}), \quad (\text{E4})$$

where $\alpha_{\Phi_i}^l$ is defined by the solutions to the eigenvalue equation $N \lambda_\Phi \alpha_\Phi = K_F \alpha_\Phi$.

It is important to stress that all the arguments shown in this appendix rely on the assumption that the data are centered in feature space. Where the centered kernel matrix, \widetilde{K}_F , can be expressed in terms of the non-centered kernel matrix, K_F , as

$$\widetilde{K}_F = K_F - 1_N K_F - K_F 1_N + 1_M K_F 1_N, \quad (\text{E5})$$

where $(1_N)_{ij} = 1/N$. The reader should be aware that we always refer to the centered kernel matrix \widetilde{K}_F . However, for the sake of simplicity, the tilde is not used in our notation.

Finally, we need to choose a form for the kernel function $k(\mathbf{x}_i, \mathbf{x}_j) := K_{F_{ij}}$. For the sake of simplicity, we make an *a priori* choice of using a Gaussian kernel,

$$k(\mathbf{x}_i, \mathbf{x}_j) = \exp \left[-\frac{\|\mathbf{x}_i - \mathbf{x}_j\|^2}{2\sigma^2} \right], \quad (\text{E6})$$

where the value of σ is determined by a cross-validation process.

E2 The k -Nearest Neighbor algorithm

The kNN begins with the training sample organized as $q_i = (x_i, y_i)$, where x_i is the i -th data vector and y_i its label, and a definition of distance between 2 data vectors $d(x_i, x_j)$. Given a new unlabelled test point $q_t(x_t)$, the algorithm computes the distance between x_t and all the other points in the training sample, $d(x_t, \mathbf{x})$, ordering them from lower to higher distance. The labels of the first k data vectors (the ones closer to x_t) are counted as votes in the definition of y_t . Finally, y_t is set as the label with highest number

of votes. Throughout our analysis, we used an Euclidean distance metric and order $k = 1$.

E3 Cross-validation

The main idea behind the cross-validation procedure is to remove a random set of M data points, T^{out} from the sample. The remaining part is given as input for a given classifier algorithm and used to classify the points in T^{out} . In this way, we can measure the success rate of the classifier over different random choices of T^{out} and also compare results from different classifiers given the same training and T^{out} sets (see e.g., Arlot & Celisse 2010).

The number of points in T^{out} is a free parameter and must be defined based on the clustering characteristics of the given data set. Here we chose the most classical exhaustive data splitting procedure, sometimes called *Leave One Out* (LOO) algorithm. As the name states, we construct N sub-samples T^{out} , each one containing only one data point, $M = 1$. The training sample is then cross-validated and the performance judged by the average number of correct classifications.

Data exhaustive algorithms like LOO have a larger variance in the final results, although, they are highly recommended for avoiding biases regarding local data clustering and some non-uniform geometrical distribution of data points in a given parameter space.

REFERENCES

- Abel T., Anninos P., Zhang Y., Norman M. L., 1997, *New Astronomy*, 2, 181
- Abel T., Bryan G. L., Norman M. L., 2002, *Science*, 295, 93
- Abramowitz M., Stegun I. A., 1965, *Handbook of Mathematical Functions with Formulas, Graphs and Mathematical Tables*. Dover Publications, Inc., New York
- Ahn K., Shapiro P. R., Iliev I. T., Mellema G., Pen U.-L., 2009, *ApJ*, 695, 1430
- Almgren A. S., Beckner V. E., Bell J. B., Day M. S., Howell L. H., Joggerst C. C., Lijewski M. J., Nonaka A., Singer M., Zingale M., 2010, *ApJ*, 715, 1221
- Arlot S., Celisse A., 2010, *Statistics Surveys*, 4, 40
- Barkana R., Loeb A., 2004, *ApJ*, 609, 474
- Bastian N., Covey K. R., Meyer M. R., 2010, *ARA&A*, 48, 339
- Becker R. A., Cleveland W. S., Shyu M.-J., 1996, *Journal of Computational and Graphical Statistics*, 5, 123
- Beckwith S. V. W., Stiavelli M., Koekemoer A. M., Caldwell J. A. R., Ferguson H. C., Hook R., Lucas R. A., Bergeron L. E., Corbin M., Jogee S., Panagia N., Robberto M., Royle P., Somerville R. S., Sosey M., 2006, *AJ*, 132, 1729
- Beers T. C., Christlieb N., 2005, *ARA&A*, 43, 531
- Biffi V., Maio U., 2013, *MNRAS*, 436, 1621
- Bolton J. S., Haehnelt M. G., 2013, *MNRAS*, 429, 1695
- Bromm V., 2013, *Reports on Progress in Physics*, 76, 112901
- Bromm V., Ferrara A., Coppi P. S., Larson R. B., 2001, *MNRAS*, 328, 969
- Bromm V., Loeb A., 2004, *A&A*, 9, 353
- Bromm V., Loeb A., 2006, *ApJ*, 642, 382
- Caffau E., Bonifacio P., François P., Spite M., Spite F., Zaggia S., Ludwig H.-G., Steffen M., Mashonkina L., Monaco L., Sbordone L., Molaro P., Cayrel R., Plez B., Hill V., Hammer F., Randich S., 2012, *A&A*, 542, A51
- Campisi M. A., Maio U., Salvaterra R., Ciardi B., 2011, *MNRAS*, 416, 2760
- Cayrel R., Depagne E., Spite M., Hill V., Spite F., François P., Plez B., Beers T., Primas F., Andersen J., Barbuy B., Bonifacio P., Molaro P., Nordström B., 2004, *A&A*, 416, 1117
- Chatzopoulos E., Wheeler J. C., 2012, *ApJ*, 748, 42
- Ciardi B., Bolton J. S., Maselli A., Graziani L., 2012, *MNRAS*, 423, 558
- Clark P. C., Glover S. C. O., Smith R. J., Greif T. H., Klessen R. S., Bromm V., 2011, *Science*, 331, 1040
- Cohen J., 1988, *Statistical Power Analysis for the Behavioral Sciences* (2nd Edition), 2 edn. Routledge
- Cooke J., Sullivan M., Gal-Yam A., Barton E. J., Carlberg R. G., Ryan-Weber E. V., Horst C., Omori Y., Díaz C. G., 2012, *Nature*, 491, 228
- de Souza R. S., Ciardi B., Maio U., Ferrara A., 2013a, *MNRAS*, 428, 2109
- de Souza R. S., Ishida E. E. O., Johnson J. L., Whalen D. J., Mesinger A., 2013b, *MNRAS*, 436, 1555
- de Souza R. S., Krone-Martins A., Ishida E. E. O., Ciardi B., 2012, *A&A*, 545, A102
- de Souza R. S., Maio U., Biffi V., Ciardi B., 2013c, *astro-ph/1308.6009*
- de Souza R. S., Yoshida N., Ioka K., 2011, *A&A*, 533, A32
- Dessart L., Waldman R., Livne E., Hillier D. J., Blondin S., 2013, *MNRAS*, 428, 3227
- Dijkstra M., Haiman Z., Mesinger A., Wyithe J. S. B., 2008, *MNRAS*, 391, 1961
- Frebel A., Aoki W., Christlieb N., Ando H., Asplund M., Barklem P. S., Beers T. C., Eriksson K., et al. 2005, *Nature*, 434, 871
- Frey L. H., Even W., Whalen D. J., Fryer C. L., Hungerford A. L., Fontes C. J., Colgan J., 2013, *ApJS*, 204, 16
- Gal-Yam A., Mazzali P., Ofek E. O., Nugent P. E., Kulkarni S. R., Kasliwal M. M., Quimby R. M., Filippenko A. V., et al. 2009, *Nature*, 462, 624
- Galli D., Palla F., 1998, *A&A*, 335, 403
- Gardner J. P., Mather J. C., Clampin M., Doyon R., Greenhouse M. A., Hammel H. B., Hutchings J. B., Jakobsen P., et al. 2006, *Space Sci. Rev.*, 123, 485
- Gittings M., Weaver R., Clover M., Betlach T., Byrne N., Coker R., Dendy E., Hueckstaedt R., New K., Oakes W. R., Ranta D., Stefan R., 2008, *Computational Science and Discovery*, 1, 015005
- Goodman S., 2008, *Seminars in hematology*, 45, 135
- Greif T. H., Springel V., White S. D. M., Glover S. C. O., Clark P. C., Smith R. J., Klessen R. S., Bromm V., 2011, *ApJ*, 737, 75
- Gunn J. E., Peterson B. A., 1965, *ApJ*, 142, 1633
- Harrison C. M., Meiksin A., Stock D., 2011, *astro-ph/1105.6208*
- Hasegawa K., Semelin B., 2013, *MNRAS*, 428, 154
- Heger A., Woosley S. E., 2002, *ApJ*, 567, 532
- Heger A., Woosley S. E., 2010, *ApJ*, 724, 341
- Hillebrandt W., Niemeyer J. C., 2000, *ARA&A*, 38, 191
- Hirano S., Hosokawa T., Yoshida N., Umeda H., Omukai K., Chiaki G., Yorke H. W., 2013, *arXiv:1308.4456*
- Hosokawa T., Omukai K., Yoshida N., Yorke H. W., 2011, *Science*, 334, 1250
- Hummel J. A., Pawlik A. H., Milosavljević M., Bromm V., 2012, *ApJ*, 755, 72
- Ishida E. E. O., de Souza R. S., 2013, *MNRAS*, 430, 509
- Ishida E. E. O., de Souza R. S., Ferrara A., 2011, *MNRAS*, 418, 500
- Iwamoto N., Umeda H., Tominaga N., Nomoto K., Maeda K., 2005, *Science*, 309, 451
- Joggerst C. C., Almgren A., Bell J., Heger A., Whalen D.,

- Woosley S. E., 2010, *ApJ*, 709, 11
- Joggerst C. C., Whalen D. J., 2011, *ApJ*, 728, 129
- Johnson J. L., Dalla Vecchia C., Khochfar S., 2013a, *MNRAS*, 428, 1857
- Johnson J. L., Whalen D. J., Even W., Fryer C. L., Heger A., Smidt J., Chen K.-J., 2013, *ApJ*, 775, 107
- Kanyongo G. Y., Brook G. P., Kyei-Blankson L., Gocmen G., 2007, *Journal of Modern Applied Statistical Methods*, 6, 81
- Karlsson T., Bromm V., Bland-Hawthorn J., 2013, *Reviews of Modern Physics*, 85, 809
- Karlsson T., Johnson J. L., Bromm V., 2008, *ApJ*, 679, 6
- Karpenka N. V., Feroz F., Hobson M. P., 2012, *ArXiv e-prints*
- Kasen D., Woosley S. E., 2009, *ApJ*, 703, 2205
- Kasen D., Woosley S. E., Heger A., 2011, *ApJ*, 734, 102
- Kessler R., Bassett B., Belov P., Bhatnagar V., Campbell H., Conley A., Frieman J. A., Glazov A., et al. 2010, *PASP*, 122, 1415
- Kessler R., Bernstein J. P., Cinabro D., Dilday B., Frieman J. A., Jha S., Kuhlmann S., Miknaitis G., Sako M., Taylor M., Vanderplas J., 2009, *PASP*, 121, 1028
- Komatsu E., Dunkley J., Nolte M. R., Bennett C. L., Gold B., Hinshaw G., Jarosik N., Larson D., Limon M., Page L., Spergel D. N., Halpern M., Hill R. S., Kogut A., Meyer S. S., Tucker G. S., Weiland J. L., Wollack E., Wright E. L., 2009, *ApJS*, 180, 330
- Kuncarayakti H., Doi M., Aldering G., Arimoto N., Maeda K., Morokuma T., Pereira R., Usuda T., Hashiba Y., 2013, *AJ*, 146, 31
- Kunz M., Bassett B. A., Hlozek R. A., 2007, *Phys. Rev. D*, 75, 103508
- Kuznetsova N. V., Connolly B. M., 2007, *ApJ*, 659, 530
- Lai D. K., Bolte M., Johnson J. A., Lucatello S., Heger A., Woosley S. E., 2008, *ApJ*, 681, 1524
- Mackey J., Bromm V., Hernquist L., 2003, *ApJ*, 586, 1
- Magee N. H., Abdallah Jr. J., Clark R. E. H., Cohen J. S., Collins L. A., Csanak G., Fontes C. J., Gauger A., Keady J. J., Kilcrease D. P., Merts A. L., 1995, in S. J. Adelman & W. L. Wiese ed., *Astrophysical Applications of Powerful New Databases Vol. 78 of Astronomical Society of the Pacific Conference Series, Atomic Structure Calculations and New LOS Alamos Astrophysical Opacities*. p. 51
- Maio U., Ciardi B., Dolag K., Tornatore L., Khochfar S., 2010, *MNRAS*, 407, 1003
- Maio U., Dolag K., Ciardi B., Tornatore L., 2007, *MNRAS*, 379, 963
- Maio U., Iannuzzi F., 2011, *MNRAS*, 415, 3021
- Maoz D., Mannucci F., Nelemans G., 2013, *astro-ph/1312.0628*
- Meiksin A., 2006, *MNRAS*, 365, 807
- Meiksin A., Whalen D. J., 2013, *MNRAS*, 430, 2854
- Mesinger A., Furlanetto S. R., 2008, *MNRAS*, 385, 1348
- Mesinger A., Haiman Z., Cen R., 2004, *ApJ*, 613, 23
- Mesinger A., Johnson B. D., Haiman Z., 2006, *ApJ*, 637, 80
- Mesler R. A., Whalen D. J., Lloyd-Ronning N. M., Fryer C. L., Pihlström Y. M., 2013, *The First Gamma-Ray Bursts in the Universe*, *ApJ*, in prep
- Miralda-Escude J., 1998, *ApJ*, 501, 15
- Muratov A. L., Gnedin O. Y., Gnedin N. Y., Zemp M., 2013, *ApJ*, 773, 19
- Nagakura H., Suwa Y., Ioka K., 2012, *ApJ*, 754, 85
- Newling J., Varughese M., Bassett B., Campbell H., Hlozek R., Kunz M., Lampeitl H., Martin B., Nichol R., Parkinson D., Smith M., 2011, *MNRAS*, 414, 1987
- Omukai K., Palla F., 2001, *ApJ*, 561, L55
- Omukai K., Palla F., 2003, *ApJ*, 589, 677
- Pan T., Kasen D., Loeb A., 2012, *MNRAS*, 422, 2701
- Pawlik A. H., Milosavljević M., Bromm V., 2013, *ApJ*, 767, 59
- Poznanski D., Maoz D., Gal-Yam A., 2007, *AJ*, 134, 1285
- Quimby R. M., Yuan F., Akerlof C., Wheeler J. C., 2013, *MNRAS*, 431, 912
- Richards J. W., Homrighausen D., Freeman P. E., Schafer C. M., Poznanski D., 2012, *MNRAS*, 419, 1121
- Robertson B. E., Ellis R. S., 2012, *ApJ*, 744, 95
- Robertson B. E., Ellis R. S., Dunlop J. S., McLure R. J., Stark D. P., 2010, *Nature*, 468, 49
- Rodney S. A., Tonry J. L., 2009, *ApJ*, 707, 1064
- Rydberg C.-E., Zackrisson E., Lundqvist P., Scott P., 2013, *MNRAS*, 429, 3658
- Sako M., et al. 2008, *AJ*, 135, 348
- Sako M., Bassett B., Connolly B., Dilday B., Campbell H., Frieman J. A., Gladney L., Kessler R., et al. 2011, *ApJ*, 738, 162
- Salpeter E. E., 1955, *ApJ*, 121, 161
- Schaye J., Dalla Vecchia C., Booth C. M., Wiersma R. P. C., Theuns T., Haas M. R., Bertone S., Duffy A. R., McCarthy I. G., van de Voort F., 2010, *MNRAS*, 402, 1536
- Schlegel D. J., Finkbeiner D. P., Davis M., 1998, *ApJ*, 500, 525
- Schneider R., Ferrara A., Natarajan P., Omukai K., 2002, *ApJ*, 571, 30
- Smidt J., Whalen D. J., Even W., Wiggins B., Johnson J., Stiavelli M., Fryer C. L., 2013, *Population III Hypernovae*, *ApJ*, in prep
- Springel V., 2005, *MNRAS*, 364, 1105
- Springel V., Yoshida N., White S. D. M., 2001, *New Astronomy*, 6, 79
- Stacy A., Bromm V., 2013, *astro-ph/1307.1798*
- Stacy A., Greif T. H., Bromm V., 2012, *MNRAS*, 422, 290
- Sullivan M., et al. 2006, *AJ*, 131, 960
- Tanaka M., Moriya T. J., Yoshida N., 2013, *MNRAS*, 435, 2483
- Tanaka M., Moriya T. J., Yoshida N., Nomoto K., 2012, *MNRAS*, 422, 2675
- Tornatore L., Ferrara A., Schneider R., 2007, *MNRAS*, 382, 945
- Trenti M., Stiavelli M., 2009, *ApJ*, 694, 879
- Wang B., Han Z., 2012, *NewAR*, 56, 122
- Weaver T. A., Zimmerman G. B., Woosley S. E., 1978, *ApJ*, 225, 1021
- Weinmann S. M., Lilly S. J., 2005, *ApJ*, 624, 526
- Whalen D., van Veelen B., O'Shea B. W., Norman M. L., 2008, *ApJ*, 682, 49
- Whalen D. J., Chatzopoulos M., Smidt J., Even W., Wiggins B., Johnson J., Stiavelli M., Fryer C. L., 2013g, *Finding the First Cosmic Explosions V: 85 - 135 M_{\odot} Pair-Instability Supernovae*, *ApJ*, in prep
- Whalen D. J., Even W., Frey L. H., Smidt J., Johnson J. L., Lovekin C. C., Fryer C. L., Stiavelli M., Holz D. E., Heger A., Woosley S. E., Hungerford A. L., 2013a, *ApJ*, 777, 110
- Whalen D. J., Even W., Lovekin C. C., Fryer C. L., Stiavelli M., Roming P. W. A., Cooke J., Pritchard T. A., Holz D. E., Knight C., 2013d, *ApJ*, 768, 195
- Whalen D. J., Even W., Smidt J., Heger A., Chen K.-J., Fryer C. L., Stiavelli M., Xu H., Joggerst C. C., 2013h, *ApJ*, 778, 17
- Whalen D. J., Fryer C. L., Holz D. E., Heger A., Woosley S. E., Stiavelli M., Even W., Frey L. H., 2013b, *ApJ*, 762, L6
- Whalen D. J., Joggerst C. C., Fryer C. L., Stiavelli M., Heger A., Holz D. E., 2013c, *ApJ*, 768, 95
- Whalen D. J., Smidt J., Even W., Woosley S. E., Heger A., Stiavelli M., Fryer C. L., 2013f, *arXiv:1311.1221*
- Whalen D. J., Smidt J., Johnson J. L., Holz D. E., Stiavelli M.,

- Fryer C. L., 2013e, astro-ph/1312.6330
- Wiersma R. P. C., Schaye J., Smith B. D., 2009, MNRAS, 393, 99
- Wise J. H., Abel T., 2005, ApJ, 629, 615
- Wise J. H., Turk M. J., Norman M. L., Abel T., 2012, ApJ, 745, 50
- Wolcott-Green J., Haiman Z., Bryan G. L., 2011, MNRAS, 418, 838
- Woosley S. E., Blinnikov S., Heger A., 2007, Nature, 450, 390
- Woosley S. E., Heger A., Weaver T. A., 2002, Reviews of Modern Physics, 74, 1015
- Xu H., Wise J. H., Norman M. L., 2013, ApJ, 773, 83
- Yoshida N., Omukai K., Hernquist L., Abel T., 2006, ApJ, 652, 6
- Young D. R., Smartt S. J., Valenti S., Pastorello A., Benetti S., Benn C. R., Bersier D., Botticella M. T., et al. 2010, A&A, 512, A70
- Zhang J., Yu K. F., 1998, JAMA, 280, 1690